The inflammasome adaptor protein ASC present differential intracellular and extracellular functions to trigger immunometabolic dysregulation and dysbiosis during obesity

Authors: Juan José Martinez-Garcia[1,2,3*], Sara Rodríguez[1], Adriana Guijarro[1], Ignacio Quevedo-Romero[1], Sandra V. Mateo[1], Cristina Molina-López[1,4], Laura Hurtado-Navarro[1,5], Alberto Baroja-Mazo[1], Pablo Pelegrin[1,2*].

Affiliations:

[1]Molecular Inflammation Group, Biomedical Research Institute of Murcia (IMIB), Murcia, Spain

[2]Department of Biochemistry and Molecular Biology B and Immunology, Faculty of Medicine, University of Murcia, Murcia, Spain

[3]Current address: Microbiology and Immunology Laboratory, Immunology Frontiers Research Center (IFReC), Osaka University, Osaka, Japan

[4]Current address: Metabolism, Immunology and Cardiovascular risk Group, Andalusian Molecular Biology and Regenerative Medicine Centre (CABIMER), 41092 Seville, Spain.

[5]Current address: The Innate Immune Response Group, IdiPAZ, La Paz University Hospital, Madrid, Spain.

*Correspondence to: jjmartinezgarciaio@gmail.com and pablopel@um.es

Running title: ASC controls immunometabolism in obesity

Abstract

The inflammasomes are a component of the innate immune system that induce inflammation after activation by danger and pathogen signals, this process is of extreme importance in the gut, where high-saturated fat diets modulate inflammasome activity resulting in dysbiosis and inflammation. In this work, we found that the common inflammasome adaptor protein, apoptosis speck-like protein with a caspase activation domain (ASC), is essential for the development of metabolic dysregulation during high fat diet. ASC-deficient mice (*Pycard*$^{-/-}$) presented lower weight gain and improved glucose tolerance, enhancing metabolism, and reducing inflammation in both intestine and liver. The extracellular administration of ASC oligomers to *Pycard*$^{-/-}$ mice partially rescued dysbiosis, intestinal metabolism and inflammation. Therefore, ASC presents intracellular functions activating the inflammasome, as well as extracellular function as an oligomer during metabolic dysregulation, emerging ASC as a potential drug target beneficial to treat obesity and metabolism-associated liver diseases.

Keywords: ASC, inflammasome, microbiota, metabolism, glucose tolerance, macrophages, intestinal permeability, high-fat-diet

Abbreviations list.

ASC: Apoptosis-associated Speck-like protein containing a CARD; cDNA: Complementary Deoxyribonucleic Acid; DEG: Differential Expressed Gene; DNA: Deoxyribonucleic Acid; FDR: False Discovery Rate; GO: Gene Ontology; GSDMD: Gasdermin D; GTT: Glucose Tolerance Test; HFD: High-Fat-Diet; IL: Interleukin; LPS: Lipopolysaccharide; mRNA: Messenger Ribonucleic Acid; NCD: Normal-Chow-Diet; NIN1: Ninjurin-1; NLR: Nucleotide-binding domain Leucine-rich Repeat receptor; NLRP: Nucleotide-binding domain Leucine-rich Repeat Pyrin domain-containing receptor; NOD: Nucleotide-binding and Oligomerization Domain; PCA: Principal Components Analysis; PCR: Polymerase Chain Reaction; PBS: Phosphate Saline Buffer; RNA: Ribonucleic Acid; TCA: Tricarboxylic Acids cycle; TLR: Toll-Like Receptor; ZT: Zeitgeber Time.

Introduction

Nucleotide-binding domain leucine-rich repeat receptors (NLRs) constitute an important part of the inflammatory response, responding to a wide variety of danger and pathogens associated molecular patterns (1,2). NLRs, including the most studied NLRP3, are highly expressed in immune myeloid cells as well as in epithelial cells (3). NLRP3 and other NLRs can oligomerize forming inflammasomes that activate caspase-1 to mature the proinflammatory cytokines interleukin (IL)-1β and IL-18 (4,5). Caspase-1 also processes the protein gasdermin D (GSDMD), which N-terminal fragment form pores in the plasma membrane initiating the release of IL-1β and IL-18 and induces an immunogenic programmed cell death termed pyroptosis (6). During pyroptotic cell death the plasma membrane protein ninjurin-1 (NINJ1) induces membrane rupture (7). Most of the inflammasomes require interaction and oligomerization of the apoptosis-associated speck-like protein containing a caspase-1 activating domain (ASC) to activate caspase-1. Inflammasome oligomers of ASC are externalized to the extracellular milieu during pyroptosis to amplify the inflammatory response (8,9). Thus, beyond the intracellular scaffold function of ASC to recruit and activate caspase-1, extracellular ASC oligomers play a role in different pathologies amplifying the inflammatory response and causing amyloid deposition (10–13).

Intestinal microbiota plays a crucial role contributing to the host's health and survival (14). This makes the gut extremely sensitive to microbiota changes, which controls colonisation by opportunistic bacteria and triggers innate immune responses, including inflammation (15,16). Subsequently, the effect of the gut microbiome controlling the activity of the inflammasome has been reported with both antibiotics and germ-free (GF) conditions (17,18). The participation of the different inflammasomes, including the NLRP3, has been tightly associated with diet-related metabolic diseases, such as obesity and type II diabetes (19). In fact, the consume of diets with high saturated fats (HFD) induces an inflammatory response and increase IL-1β production (20). Furthermore, the NLRP6 inflammasome, which is present in epithelial intestinal cells, maintains gut microbiota homeostasis through the production of IL-18 (21). Furthermore, the participation of pyroptosis induced by GSDMD has been described as a protective agent that controls intestinal microbiota and repairs intestinal mucosa (22). However, there is controversy with the role of pyroptosis in obesity, as it is not only associated with an increase in body weight but is also capable of inducing metabolic dysregulations, such as blockage of cholesterol transport for subsequent catabolic processes, the accumulation of

82 atheroma plaques, and the development of inflammatory diseases such as steatohepatitis (23–
83 25). Since there is a clear involvement of different inflammasomes in metabolic dysregulation,
84 the role of the common inflammasome adaptor protein ASC, and its intracellular and
85 extracellular functions in this disease is not fully understood. In this study we focus on the
86 effect of ASC deficiency on metabolic dysregulation induced by HFD and uncover a
87 differential function of ASC, acting as intracellular scaffold to form inflammasome and its
88 extracellular function as ASC oligomers. We identify that the deletion of ASC protects mice
89 in response to a HFD, increase the tolerance to glucose and exacerbate glycolytic and aerobic
90 metabolism in HFD conditions, with a decreased inflammatory response. ASC deficiency also
91 affected gut epithelial integrity and permeability, regulating gut microbiome. Extracellular
92 ASC oligomers administration in ASC-deficient mice partially revert dysbiosis, intestinal
93 metabolism and inflammation, revealing a differential role of intracellular and extracellular
94 ASC in metabolic dysregulation. This work demonstrates that ASC could be a potential
95 therapeutic target to treat metabolic dysfunction associated to steatosis liver disease and type II
96 diabetes.

97 **Results**

98 ***ASC deficiency prevents glucose intolerance under high-fat-diet conditions***

99 We initially asked whether ASC deficiency can modulate weight gain in obesity after feeding with
100 a HFD. Weight of *Pycard*$^{-/-}$ was lower when compared to wild type from the third month of HFD,
101 although the weight reduction was not statistically significant **(Figure 1A)**. To monitor potential
102 weight changes during the time dependent on the inflammasome, weight from C57/BL6
103 background wild type (*Pycard*$^{+/+}$) mice and *Pycard*$^{-/-}$ mice from same age was monitored during 5
104 months in normal chow diet (NCD). We observed that the *Pycard*$^{-/-}$ mice tended to gain less weight
105 than the *Pycard*$^{+/+}$ in both males and females, but this difference was not statistically significant
106 **(Figure 1B)**. However, this tendency reveals that deficiency of ASC can prevent body weight gain,
107 and this effect was independently on the sex **(Figure 1B)**. HFD-dependent weight gain was
108 confirmed comparing HFD to NCD fed wild type mice **(Suppl. Figure 1A)**. We next analysed
109 glucose tolerance by measuring the glucose concentration after intraperitoneal glucose
110 administration in mice feed with HFD and observed an increase of glucose tolerance in the *Pycard*$^{-}$
111 $^{/-}$ mice respect to wild type mice after 3 months of HFD **(Figure 1C)** and after 5 months of HFD
112 **(Figure 1D)**. As expected, glucose intolerance was mediated by the hypercaloric diet, as HFD fed
113 mice presented higher glucose intolerance compared to NCD fed mice **(Suppl. Figure 1B).**
114 Additionally, we observed that *Pycard*$^{-/-}$ mice fed with a normal diet tended to increase glucose
115 tolerance in comparison with wild type mice **(Figure 1E)**. However, genotype-dependent
116 differences in NCD fed mice were smaller than observed in HFD mice **(Figure 1C, D)**.

117

118 ***ASC controls peritoneal cell infiltration in high-fat-diet and mediates IL-1β release***

119 We observed an increase of the total number of cells in the peritoneum upon 5 months of HFD
120 respect NCD fed wild type mice **(Figure 2A)**. To investigate inflammasome function in the
121 infiltrated peritoneal cells during HFD conditions, we cultured adherent peritoneal cells from mice
122 and measure IL-1β in cell supernatants after *in vitro* NLRP3 inflammasome activation. Peritoneal
123 cells from wild type mice fed with HFD presented NLRP3-dpenent IL-1β release just by LPS
124 treatment **(Figure 2B)**, being potentiated by nigericin in both NCD and HFD conditions **(Figure**
125 **2B)**. This suggests increase sensitivity to activate IL-1β release in peritoneal infiltrated cells in
126 mice fed with a HFD. After 5 months of HFD the *Pycard*$^{-/-}$ mice presented a higher increase of
127 peritoneal cells when compared to wild type **(Figure 2C)**, but as expected, IL-1β release in

128 peritoneal cells from *Pycard*$^{-/-}$ mice was decreased when compared to wild type cells **(Figure 2D)**.
129 Absence of IL-1β release was due to the *Pycard*$^{-/-}$ genotype and not by the HFD effect **(Suppl.**
130 **Figure 1C)**. As control, we found that IL-6 release from peritoneal cells was dependent on LPS
131 stimulation, being independent of the diet or the genotype **(Figure 2E,F, Suppl. Figure 1D)**. These
132 data suggest that the absence of ASC could reduce inflammasome-dependent peritoneal cell death
133 and IL-1β production and reduce obesity-induced inflammation.
134
135 ***ASC restricts gut microbiota biodiversity and controls intestinal permeability***
136 We next wondered if ASC could influence gut dysbiosis induced by HFD. We determined 16S
137 RNA in faeces and found that the microbiota composition changed in *Pycard*$^{-/-}$ mice fed with HFD
138 during 5 months in comparison with wild type mice **(Figure 3A-C)**. After HFD, wild type mice
139 accumulated the 97% of the abundance on the four predominant class of bacteria: Clostridia,
140 Bacilli, Verrucomicrobiae and Bacteroidia **(Figure 3A)**. Within the most abundant class of
141 bacteria that was influenced by the deficiency of ASC under HFD, we encounter an increase of
142 Clostridia, meanwhile Verrucomicrobiae class decreased on *Pycard*$^{-/-}$ HFD mice **(Figure 3B).**
143 Moreover, *Pycard*$^{-/-}$ mice presented higher percentages of relative abundance for other less
144 abundant class of bacteria, specifically on Coribacteria, Desulfovibrionia, and Deferribacteres
145 **(Figure 3B)**. As a control, we observed in a different batch of mice that wild type with NCD
146 presented low proportions of Verrucomicrobiota **(Suppl. Figure 2A)**, which strongly increased
147 after HFD **(Suppl. Figure 2B)**. The increase diversity of bacteria classes found in the *Pycard*$^{-/-}$
148 after HFD was also maintained where we analysed the different represented families of bacteria
149 from the total microbiome **(Figure 3C)**. It is particularly striking the increase of Lachnospiraceae
150 family in the *Pycard*$^{-/-}$ mice after HFD, meanwhile the mucin-degrading bacteria from the
151 Akkermansiaceae family decreased **(Figure 3C)**. We corroborated in a second batch of mice that
152 Lachnospiraceae family was increased in absence of ASC **(Suppl. Figure 3A)**. After cohousing
153 between wild type and *Pycard*$^{-/-}$ mice, genetic differences were abolished before and after the HFD
154 treatment except for an increase of Lactobacillaceae in *Pycard*$^{-/-}$ mice after HFD **(Suppl. Figure**
155 **3B,C)**. Moreover, the average of the alpha-biodiversity Shannon Index increased in *Pycard*$^{-/-}$ mice
156 after HFD **(Figure 3D)**. Within the most representative genus of bacteria, *Akkermansia* abundance
157 tended to decrease in absence of ASC **(Figure 3E)**. In a different batch of mice, we tested the
158 abundance of *Akkermansia* after a HFD in comparison with a NCD, where we observed that HFD

159 highly increased the proportion of this bacterium **(Suppl. Figure 2C)**. Contrarily to *Akkermansia*,
160 and accordingly with observed for class and families, other genus of bacteria strongly increased
161 its abundance, becoming the most abundant bacteria in the microbiome of *Pycard*$^{-/-}$ mice after
162 HFD, including *Odoribacter*, *Lachnospiraceae* NK4A136, *Coriobacteriaceae* UGC002, and
163 *Lactobacillus* **(Figure 3F-I)**. On the contrary, ASC deficiency decreased the proportion of
164 potential pathobionts such as *Streptococcus* and *Dorea* **(Figure 3J, K)**. We next evaluated
165 intestinal permeability by FITC-dextran measurement on the plasma of wild type and *Pycard*$^{-/-}$
166 mice fed with a NCD or a HFD and found that intestinal permeability increased in wild type mice
167 after HFD, but not in *Pycard*$^{-/-}$ mice **(Figure 3L)**. We validated in a second batch of mice that
168 HFD increased intestinal permeability in comparison with NCD fed mice **(Suppl. Figure 2D)**.
169 These data show that ASC deficiency prevent dysbiosis in response to HFD, maintaining a low
170 intestinal permeability, probably due to the decrease of pathobionts and mucin-degrading bacteria
171 that influence intestinal epithelial protective functions.
172
173 ***ASC facilitates bacteria attachment to intestinal villi during high-fat-diet***
174 Since the absence of ASC reduces intestinal permeability and prevents dysbiosis, we next
175 examined if the intestinal mucosa was altered after HFD. We observed that wild type mice fed
176 with HFD presented severe bacterial colonization in the small intestinal *villi* **(Figure 4A)**.
177 Additionally, exacerbated amount of mucin was observed in the lumen of the intestinal tissue,
178 meanwhile the space between *villi* presented numerous areas without mucin **(Figure 4A).**
179 Contrarily**,** bacteria attached to the *villi* decreased in *Pycard*$^{-/-}$ mice, and mucin amount was
180 controlled in the border of each intestinal *villi* and uniformly disposed **(Figure 4B)**. As a control,
181 when the intestinal *villi* of wild type mice fed with NCD were compared with the pathologic
182 phenotype of the HFD fed mice, we observed a normal intestinal histology with low bacteria in
183 the *villi* **(Suppl. Figure 2E, F)**. Regarding the uncontrolled amount of mucin found in the small
184 intestine of wild type mice, we wondered if the absence of ASC would trigger a transcriptional
185 profile to protect mucin degradation from bacteria. Bulk RNA sequencing in the small intestine of
186 mice fed with HFD showed increasing transcript levels of the β-galactoside sialyltransferases
187 encoding genes (*ST6Galnac2-6*) in *Pycard*$^{-/-}$ mice **(Figure 4C)**, which could explain the protection
188 of mucin between *villi*, being less accessible to mucin-degrading bacteria.

189 Regarding the importance of the ASC-dependent inflammasomes in glucose tolerance **(Figure**
190 **1C,D)**, we measured the amount of IL-1β in the small intestine, which was decreased in *Pycard*$^{-/-}$
191 feed with a HFD compared to wild type mice **(Figure 4D)**. Bulk RNA sequencing demonstrated
192 that the presence of ASC increased the expression of genes related to intestinal inflammation (e.g.
193 *Mertk, Smpdl3b, Fkbp5)*, epithelial integrity and mucus secretion (e.g. *Spink1, Pmaip1, Erbb3,*
194 *Sl26a6, Ern2)*, and epithelial proliferation and regeneration (e.g. *Ksr, Npas2, Sertad1, Slx1b, Ddit)*
195 **(Figure 4E)**. However, the *Pycard*$^{-/-}$ mice have increased expression of metabolic and anti-
196 inflammatory transcript genes (*Gdpd3* and *Ide*) **(Figure 4E).** Gene Ontology (GO) analysis from
197 the differential expressed genes in the small intestine revealed that meanwhile the most enriched
198 pathways in the HFD fed *Pycard*$^{-/-}$ mice were the regulation of the T cell response and the
199 regulation of the MHC class I and II activity, on *Pycard*$^{+/+}$ mice, the AIM2 and NLRP3
200 inflammasome, hormonal activity and positive regulation of the humoral immune response were
201 between the top 10 highly expressed pathways **(Figure 4F, Suppl. Figure 4)**. All together the
202 deficiency of ASC induced in the small intestine mucosa a protective mechanism during HFD,
203 reducing inflammation, increasing mucosal protection and preventing bacteria attachment to the
204 *villi*.
205
206 ***ASC deficiency increases glycolytic and mitochondrial metabolism in the small intestine during***
207 ***obesity***
208 As the RNA sequencing revealed a tendency to increase some metabolic genes under HFD
209 treatment, which could also explain the elevation of IL-1β, we then analyzed in the small intestine
210 the expression of key metabolic genes related to glycolysis and the tricarboxylic acids (TCA)
211 cycle. Interestingly, we found that the glycolytic *Pkm* gene coding for the pyruvate kinase enzyme
212 was highly expressed in the *Pycard*$^{-/-}$ mice after HFD **(Figure 5A)**. Contrarily, the anaerobic
213 respiration-related gene *Ldha*, corresponding to the enzyme lactate dehydrogenase, decreased in
214 the *Pycard*$^{-/-}$ mice **(Figure 5B)**. Consequently, we observed an increase in the expression of *Pdha*
215 gene, which encodes the pyruvate dehydrogenase enzyme **(Figure 5C)**. This observation could
216 indicate that the high glycolytic state of the small intestine in the *Pycard*$^{-/-}$ mice after HFD drives
217 to an aerobic metabolism, and not to the anaerobic pathway. To verify this switch, we also analyzed
218 the expression of enzymes implicated in mitochondrial metabolism in the small intestine, including
219 those for the TCA cycle, the oxidation of fatty acids and the catabolism of amino acids. We found

220 that the expression of *Nnt*, *Glud1* and *Sdha* genes increased in the *Pycard*$^{-/-}$ mice after HFD **(Figure**
221 **5D-F)**. We also demonstrated that the expression of the β-oxidation-related gene *Cpt1a* increased
222 in *Pycard*$^{-/-}$ mice respect to wild type mice **(Figure 5G)**. These results align with the fact that the
223 *Pycard*$^{-/-}$ have decreased weight and increased glucose tolerance independently on the HFD
224 probably due to a high catabolism and energy uptake.
225
226 ***ASC deficiency enhances hepatic metabolism and reduces inflammation and fat accumulation***
227 ***under high-fat-diet***
228 We then investigated if *Pycard*$^{-/-}$ mice have an altered liver physiopathology and metabolism
229 during HFD. Initially we observed that wild type mice fed with HFD presented an exacerbated fat
230 accumulation in the liver, with some isolated inflammatory foci **(Figure 6A)**. Contrarily, the
231 accumulation of fat in the liver was absent in ASC-deficient mice after HFD **(Figure 6B)**. The
232 accumulation of hepatic fat due to the HFD in wild type was corroborated when compared with
233 NCD fed mice **(Suppl. Figure 5A, B)**. Similarly to small intestinal mucosa, in the liver there was
234 also decreased IL-1β production in the *Pycard*$^{-/-}$ mice fed with HFD **(Figure 6C),** and no changes
235 between genotypes were observed for IL-6 **(Figure 6D).** The high hepatic increase of the
236 inflammasome-dependent cytokine IL-1β, was specific for the HFD, as NCD mice for both
237 genotypes, showed basal levels of IL-1β **(Suppl. Figure 5C, D)**. Moreover, we observed increased
238 expression of metabolic genes in the liver of *Pycard*$^{-/-}$ HFD fed mice, in particular genes related
239 with the PPARα signaling pathway, as the master energy homeostasis regulator *Pgc1a* **(Figure**
240 **6E)**. Similar to the small intestine, the mitochondrial metabolic genes *Nnt*, *Glud1* and *Sdha* were
241 more expressed in the *Pycard*$^{-/-}$ mice after HFD **(Figure 6F-H)**, and the fatty acid oxidation-related
242 gene *Cpt1a* slightly tended to increase in the absence of ASC **(Figure 6I)**. Interestingly, we
243 observed a marked increased expression of the ketone bodies-dependent gene *Hmgcs2* in *Pycard*$^{-}$
244 $^{/-}$ mice fed with a HFD **(Figure 6J)**. Overall, ASC is important for the development of the
245 metabolic syndrome induced by HFD.
246
247 ***Extracellular ASC oligomers partially control metabolic syndrome during obesity.***
248 Beyond intracellular function of ASC forming inflammasomes, ASC oligomeric particles could
249 also reach the extracellular milieu after pyroptosis being important for different pathologies (8–
250 13,26). To explore if extracellular ASC oligomers were important for the development of

251 metabolic syndrome after HFD, we rescued the *Pycard*$^{-/-}$ mice with intraperitoneal administration
252 of recombinant ASC oligomers **(Suppl. Figure 6A)**. Intestinal permeability was slightly reverted
253 by administration of recombinant ASC oligomers, but differences were not significant comparing
254 to the *Pycard*$^{+/+}$ positive control **(Figure 7A)**. The administration of recombinant ASC oligomers
255 produced a change in the gut microbiota composition of *Pycard*$^{-/-}$, which experimented a rescue to
256 an intermediate microbiome phenotype between *Pycard*$^{+/+}$ and *Pycard*$^{-/-}$ mice **(Figure 7B)**. These
257 changes included the disappearance of some important beneficial bacteria genus found in *Pycard*$^{-}$
258 $^{/-}$ mice fed with a HFD, such as *Lactobacillus* and *Coriobacteriaceae* UGC002, as well as less
259 abundant bacteria such as *Enteractinococcus* and *Atopostipes* **(Figure 7B)**. Meanwhile, other
260 bacteria such as *Oridobacter* and *Lachnospiraceae* NK4A136 maintained high abundance
261 independently on the administration of extracellular ASC oligomers **(Figure 7B)**. The decrease of
262 pathobionts found in the in *Pycard*$^{-/-}$ mice fed with a HFD was not affected by the administration
263 of recombinant ASC oligomers, but interestingly the mucin-degrading bacteria *Akkermansia*
264 tended to increase after extracellular ASC administration **(Figure 7B)**. We also observed a
265 tendency to recover the abundance pattern of the different class of bacteria observed in *Pycard*$^{+/+}$
266 mice, especially those less abundant classes, which were strongly reduced and responsible to
267 decrease the biodiversity in *Pycard*$^{-/-}$ mice after a HFD **(Suppl. Figure 6B)**. Additionally, ASC
268 oligomer administration to in *Pycard*$^{-/-}$ mice tended to recover the two most abundant families of
269 bacteria (Akkermansiaceae and Lachnospiraceae) towards wild type mice abundance percentages
270 **(Suppl. Figure 6C, D)**. This suggests that during HFD, inflammasome oligomers might be
271 eliminated by the intestine where it could impact in gut microbiota composition, creating a
272 beneficial environment in the gut by the lack of cellular free ASC oligomers. According to the
273 increasing levels of mucin-degrading bacteria after treatment with extracellular ASC oligomers,
274 we observed that this treatment also resulted in mucus not correctly attached between the *villi*
275 space when compared with the *Pycard*$^{-/-}$ mice without recombinant ASC oligomers administration
276 **(Figure 7C)**. However, we did not observe differences in the transcript expression for the
277 *ST6Galnac* gene family in the intestine **(Figure 7D)**.
278 The administration of recombinant ASC specks in *Pycard*$^{-/-}$ mice during HFD induced a partial
279 reversion of the expression of some genes in the intestinal epithelia, especially those genes related
280 to mitochondrial catabolism **(Figure 7E)**. Furthermore, bulk RNA-sequencing in the intestinal
281 tissue revealed that extracellular ASC treatment of *Pycard*$^{-/-}$ mice during HFD resulted in

282 intermediate transcriptional profile between the wild type and the non-treated *Pycard*$^{-/-}$ mice
283 **(Figure 7F)**. As expected, intraperitoneal administration of recombinant ASC oligomers reverted
284 IL-1β in the small intestine **(Figure 7G)**, confirming previous research where extracellular ASC
285 oligomers could be internalized by macrophages and reconstitute inflammasome activity (8). We
286 then confirmed that ASC gene expression was absent during the administration of recombinant
287 ASC oligomers in the *Pycard*$^{-/-}$ mice **(Figure 7H)**, confirming that the phenotype observed was
288 independent of the endogenous expression of ASC.
289 ASC intraperitoneal treatment did not affect weight gain or glucose tolerance **(Suppl. Figure 7A,**
290 **B)**. However, administration of ASC oligomers under HFD induced a tendency to increase the
291 maximum peak of glycemia at 20 minutes after glucose injection in *Pycard*$^{-/-}$ mice **(Suppl. Figure**
292 **7B)**. In addition, differentially to the effects observed in the small intestine, intraperitoneal
293 administration of recombinant ASC oligomers did not rescue wild type phenotype of hepatic
294 damage and fat accumulation after a HFD **(Suppl. Figure 7C, D)**, and similar low levels of hepatic
295 IL-1β and high hepatic metabolism were also found after administration of ASC recombinant
296 oligomers in the *Pycard*$^{-/-}$ mice **(Suppl. Figure 7E, F)**. This suggests that extracellular ASC
297 oligomers impact at the level of the small intestine, but not in hepatic physiopathology
298 consequences, that might be controlled by the intracellular function of ASC-dependent
299 inflammasomes or its downstream consequences.
300 Overall, ASC-dependent inflammasomes control metabolic syndrome induced by HFD at different
301 levels, modulating intestinal permeability and inflammation, dysbiosis, glucose tolerance, hepatic
302 inflammation, metabolism and steatosis. The presence of extracellular ASC oligomers partially
303 modulates these effects but mainly impacted in dysbiosis and small intestine metabolism and
304 inflammation.

305 **Discussion**

306 In this study we found that ASC deficiency presented a protective effect during obesity induced
307 metabolic syndrome. This protection was observed at different levels, including the decrease of
308 intestinal permeability, dysbiosis, changes in the integrity, metagenomic, metabolism and
309 physiology of the small intestine epithelia, and a decrease of IL-1β production. This protective
310 effect was also found in hepatic metabolism, inflammation and steatosis. Dysbiosis, intestinal
311 metabolism and IL-1β production were reverted in the *Pycard*$^{-/-}$ mice when recombinant ASC
312 oligomers were intraperitoneally administrated during the HFD, suggesting a differential role of
313 extracellular ASC oligomers for microbiota and intestine and hepatic functions.

314 Our study is in line with a previous study where ASC was also found able to regulate glucose
315 tolerance in obesity (27), but other studies found an ASC-independent protection of the intestinal
316 mucosa and dysbiosis that were dependent on the mother and cage (28). In this study we found
317 that obesity-induced dysbiosis was partially reverted by administration of extracellular ASC
318 oligomers, and cohousing demonstrated that specifically the presence ASC influences dysbiosis
319 during HFD. This suggests that certain differences in microbiota composition can be explained by
320 the cage or the mother, but our results support changes in the intestinal microbiome dependent of
321 the extracellular presence of ASC during HFD. Additionally, previous studies used a HFD
322 composition of 60% Kcal fat content (27), and humans that ingest high fat in westernized diets
323 does not usually reach 40% Kcal in fat consumption (29,30). Our model with a 45% Kcal in
324 saturated fat content is focused to mimic the human physiopathology of obesity and could
325 contribute to potential differences with other studies.

326 Intestinal permeability has been related to the composition of the gut microbiota (31), and our
327 results supported this idea as HFD impact intestinal microbiota biodiversity. HFD increase the
328 abundance of species of the Verrucomicrobiae class, including *Akkermansia* genus, and
329 specifically *A. muciniphila,* a mucin-degrading bacteria which normally is beneficial for the gut,
330 but in excess, it can dysregulate gut homeostasis (32–34). However, the pathological consequences
331 of HFD could not be attributed exclusively to *Akkermansia* abundance. It is reported that gut
332 pathobionts have an advantageous niche when highly increased *Akkermansia* degrades mucus (35).
333 Our results revealed that endogenous ASC was associated with the growing of *Dorea,* which could
334 be considered a pathobiont (36). Also, we observed *Streptococcus* increase in an ASC-dependent
335 manner, but the relationship between *Streptococcus* genera and the host is more complex and

336 depends on the specie studied (37–39). Moreover, the decrease of *Akkermansia* in the gut create a
337 new niche that can be colonised other by less abundant bacteria, reducing dysbiosis and increasing
338 the microbial biodiversity as we observe for the *Pycard*$^{-/-}$ HFD fed mice group. The decrease in
339 mucus production could reduce the attachment of segmented filamentous bacteria, which then
340 induces an immune response to maintain homeostasis of the intestinal mucosa (40). In our study,
341 we also found high abundance of *Odoribacter* in ASC deficient mice, which is known to control
342 glucose levels and inflammation (41). The protection of dysbiosis by the deficiency of ASC was
343 also corroborated at histological level, where lack of ASC prevented the inclusion of bacteria in
344 the intestinal mucosa, with an increase of mucus between the intestinal *villi*. Additionally,
345 administration of recombinant ASC oligomers rescued the phenotype of ASC-deficient mice at
346 intestinal level and promoted a dysbiosis similar to the wild type mice during HFD, reducing also
347 intestinal mucus layer. Indeed, intestinal gene expression showed an increase of the *ST6Galnac*
348 gene family in ASC deficient mice, being these genes codifying for a family of sialyl-transferases
349 which induces mucus sialylation and promoting intestinal mucosa protection from bacterial
350 degradation (42). Especially, we observe a partial reversion of *ST6Galnac6* expression after
351 administration of ASC oligomers, which is specifically important to protect the mucosa from
352 bacterial invasion (43). Concomitantly with this effect, we also found that ASC controlled
353 intestinal epithelia gene expression related with the innate immune response against pathogens,
354 inflammation, and epithelial integrity, some of them are considered as markers for obesity and
355 cancer (44,45). Moreover, the increasing expression of the insulin degrading enzyme (*Ide*) gene
356 that we observed in *Pycard*$^{-/-}$ mice under HFD could explain the increasing tolerance to glucose,
357 as this enzyme protects from insulin resistance, and obesity in response to high glycemia levels
358 (46,47). Additionally, we found that the intestinal production of IL-1β dependent on ASC might
359 be attributed to the NLRP3 inflammasome activation, as previous studies have found the
360 participation of NLRP3 during obesity (17,48). However, we did not discard the participation of
361 other inflammasomes, which are also dependent on ASC and expressed in intestinal epithelia, that
362 could contribute to IL-1β production (49–51).
363 ASC oligomers have been detected extracellularly in different pathologies, including
364 autoinflammatory syndromes, amyloidosis, Alzheimer disease, and HIV infection (8–13,26).
365 However, we found that obesity, glucose tolerance and liver steatosis, long term pathological
366 consequences of metabolic syndrome (52,53), were not affected by the presence of extracellular

367 ASC oligomers, which being probably dependent on the intracellular functions of ASC. In fact,
368 we found an increase of peritoneal cells in the absence of ASC, probably as consequence of the
369 reduced cell death of peritoneal cells upon ASC-dependent inflammasome activation (54).
370 Therefore, the protective effect of ASC depletion could be mediated by a mechanism of regulation
371 which depends on the inflammasome induced ASC oligomerization, being the release of these
372 oligomers controlling additional pathological consequences during obesity. Recent developments
373 of nanobodies-targeting extracellular ASC oligomers (12) might be beneficial to treat dysbiosis
374 associated to HFD. Additionally, metabolic syndrome could be controlled by conventional
375 antibodies targeting ASC or other small molecules blocking ASC oligomerization have been
376 shown to reduce inflammation in different models (55–59). This is of relevance, as multiple
377 inflammasomes have been involved in the pathophysiology of metabolic syndrome (49,60–62),
378 and targeting ASC could modulate all of them with a single drug that could go beyond
379 inflammasome or IL-1 blocking therapies (63,64). Particularly, we found that small intestinal cells
380 presented an exacerbated catabolic pathway in *Pycard*$^{-/-}$ mice. This might be due because of the
381 increased glucose tolerance with an augmented glycolytic pathway and TCA through the enzyme's
382 pyruvate kinase and pyruvate dehydrogenase, while decreasing anaerobic lactate dehydrogenase
383 activity. This regulation of glycolysis would reduce fat accumulation in the liver and might
384 increase hepatic metabolism (65). The increased metabolism found in the liver could be the
385 consequence to reduce fat accumulation, in a very similar manner as occurs for the small intestine.
386 However, differentially to the small intestine, extracellular ASC oligomers did not rescue the
387 pathological phenotype of the liver.
388 In summary, we report a mechanism of protection to the hyperglycaemic, westernized and high-
389 saturated fat diets which is dependent on the deficiency of the inflammasome adaptor protein ASC.
390 This mechanism is characterized by an exacerbated glucose metabolism together an increasing
391 inflammatory phenotype and a decreasing intestinal permeability by the prevention of dysbiosis
392 and mucus degradation. Extracellular ASC have a specific role on the development of the mucosal
393 immunology and dysbiosis during HFD, but not in the systemic consequences of metabolic
394 syndrome, including hepatic function, tolerance to glucose, and weight gain, which appear to be
395 controlled by the intracellular ASC function forming inflammasomes. Further studies are
396 warranted to evaluate potential therapeutic approximations based in the inhibition of ASC
397 oligomerization.

398 **Materials and Methods**

399

400 ***Animal Models.*** Animal studies were approved by the Animal Health Service of the General
401 Directorate of Farming, Fishing and Aquiculture of the Council of Murcia (CARM, ID#
402 A13211201) once were positively evaluated by the Animal Experimentation Ethics Committee
403 (CEEA) of the University of Murcia (#738/2021) according to the 53/2013 Royal Decree and the
404 32/2007 National Law. Mice were bred in specific pathogen-free conditions with a 12:12 h light-
405 dark cycle in the animal facility from the University of Murcia, according to governmental
406 guidelines 86/609/CEE. Age and gender-matched ASC-deficient (*Pycard*$^{-/-}$) and wild type
407 C57BL6/J (*Pycard*$^{+/+}$) backgrounds mice were provided to a free access to a standard laboratory
408 chow diet. For the obesity model, mice were fed with a 45% saturated fat HFD (D12491, Research
409 Diets). Mice were autopsied after euthanasia with excess of isoflurane and cervical dislocation
410 according to the ethical protocols of the national and international animal experimentation
411 guidelines. After sacrifice, feces, peritoneal lavage, the right lobule of the liver, 1 cm of the
412 proximal small intestine and blood samples were recovered. All samples were recovered strictly
413 in the morning between Zeitgeber Time (ZT)0 and ZT4, to avoid the interference of the circadian
414 changes. Histological samples were collected on paraformaldehyde 4% (Sigma-Aldrich,
415 Burlington, MA) at room temperature. For RTqPCR samples, tissues were collected on RNA later
416 (Qiagen, Germany) and frozen on liquid nitrogen. Feces were collected in a dry tube and frozen
417 on liquid nitrogen. Peritoneal cells were collected on Phosphate Saline Buffer (PBS) and kept at
418 4ºC before plating. Plasma was collected in heparin tubes (Microvette® CB 300 LH, Sarstedt,
419 Germany). For tissue storage, samples were stored at -80ºC.

420

421 ***In vivo treatments***. ASC Oligomers were produced and purified as we previously described in
422 Alarcón-Vila et al. 2024 (11). Counted ASC oligomers were diluted into 1x PBS at a concentration
423 of $4x10^6$ oligomers per 100µl, ready to use it *in vivo*. ASC Oligomers were weekly injected
424 intraperitoneally at a concentration of $4x10^6$ oligomers per mouse. Glucose Tolerance Test (GTT)
425 was done at 3 and 5 months after the administration of the HFD upon gender and sex matched
426 animals. Prior the GTT assay, animals were fasted the day before for 14 hours to avoid food
427 interference on the glucose levels. Basal fasted glycemia was measured before glucose
428 administration. Following, 1g/Kg of D-glucose (Sigma-Aldrich) was intraperitoneally injected to

429 each mouse, and glycemia was measured every 20 minutes for a minimum of one hour. The last
430 point was measured at 90 minutes after glucose injection. At the end of the experiment, mice were
431 fed back again. For the intestinal permeability assay, mice were deprived of drinking water during
432 one hour at ZT0. Immediately, 4 kDa FITC-dextran were administered orally by gavage at a
433 concentration of 600 mg/Kg of mouse. After one hour, blood was collected, and plasma was
434 obtained by centrifugation at 2000 x g for 8 minutes. Fluorescence at 450 nm excitation and 570
435 nm emission was measured from the plasma using a Synergy Mx plate reader (BioTek).
436
437 ***Cells and Treatments.*** $5x10^5$ peritoneal cells (lymphocytes were not included into the count) were
438 seeded per well in 24 wells plate at 1 million/mL concentration in RPMI medium (Sigma Aldrich)
439 supplemented with 10% fetal bovine serum (Biowest), 2 mM GlutaMAX (Thermo Fisher
440 Scientific) and 1% Penicillin Streptomycin (Corning). After overnight incubation at 37ºC and 5%
441 CO_2 non-adherent cells were removed and LPS from *Escherichia coli* 055:B5 (Sigma-Aldrich)
442 was added at 1 μg/mL for 4 hours in OptiMEM (Gibco). After priming, supernatant was removed
443 and nigericin (Sigma-Aldrich) was added at 10 μM in a buffer containing 147 mM NaCl, 10 mM
444 HEPES, 13 mM D-glucose, 2 mM $CaCl_2$, 1 mM $MgCl_2$, and 2 mM KCl (pH 7.4) for 30 minutes.
445 MCC950 (Sigma-Aldrich) was added simultaneously to the nigericin at 10 μM.
446
447 ***Tissue lysates preparation.*** Liver and small intestines previously stored at -80ºC were
448 mechanically lysed and kept on ice. After being centrifuged at 16,000 x g for 10 minutes,
449 supernatant was recovered, and protein concentration was determined using the Bradford reagent
450 (Sigma Aldrich).
451
452 ***ELISA determinations.*** After *in vitro* peritoneal cell stimulation, supernatants from the cells were
453 collected and centrifuged at 16,000 x g for 30 seconds. IL-1β and IL-6 were measured in the
454 peritoneal cells supernatants, as well as in the liver and small intestine soluble fractions, using the
455 mouse Quantikine™ ELISA kits, catalogue number MLB00C-1 and M6000B respectively (R&D
456 Systems, Minneapolis, MN) following the manufacturer indications, and results were analysed in
457 a Sinergy MX plate reader (BioTek, Winooski, VT).
458

459 ***Histological samples preparation and analysis.*** Fixed liver and small intestine were processed,
460 paraffin-embedded and sections stained with haematoxylin and eosin using standard methods.
461 Slides were examined using a Zeiss Axio Scope AX10 microscope with an AxioCamICC3 (Carl
462 Zeiss, Germany).
463
464 ***RNA extraction and RTqPCR determination.*** RNA was isolated using the RNeasy mini kit
465 according to the manufacturer instructions (Qiagen). Cell lysis was performed with the addition of
466 RLT buffer supplemented with β-mercaptoethanol. RNA integrity and concentration were
467 assessed using the NanoDrop spectrophotometer (Thermo Fisher Scientific, Waltham, MA)
468 Isolated RNA was reverse transcribed with the iScript™ cDNA Synthesis Kit (BioRad, Hercules,
469 CA) according to the manufacturer's instructions. The resulting complementary DNA (equivalent
470 to 500 ng of total RNA) was amplified using the mix SYBR Premix ExTaq (Takara) and detected
471 at real time on the iCyclerMyiQ thermocycler (BioRad). Quantitative PCR was performed using
472 forward and reverse primers (**Supplemental Table 1**). On completion of the PCR amplification, a
473 DNA melting curve analysis was carried out to confirm the presence of a single amplicon. *Actb*
474 gene was used as a reference gene to normalize the transcript levels. Relative mRNA levels (2^{-}
475 $^{\Delta\Delta Ct}$) were determined by comparing the ΔCt values for treated and control groups (ΔΔCt).
476
477 ***RNA library preparation and sequencing.*** RNA libraries were prepared using the QuantSeq
478 3'mRNA-Seq V2 Library Prep Kit REV with UDI Set B (Lexogen, Austria), following the
479 manufacturer's protocol. Briefly, 500 ng of total RNA per sample was used as input for poly(A)
480 mRNA capture using oligo-dT beads. Captured mRNA was fragmented and reverse-transcribed
481 into cDNA. Second-strand synthesis and adapter ligation were performed to generate double-
482 stranded cDNA libraries. Libraries were indexed with 12-nucleotide unique dual indices for
483 multiplexing and amplified using polymerase chain reaction (PCR). The quality and quantity of
484 the final libraries were evaluated using the Agilent 2100 Bioanalyzer and the Qubit 4 Fluorometer
485 (Thermo Fisher Scientific). Libraries were sequenced on a NextSeq 2000 system (Illumina, San
486 Diego, CA) in paired-end mode with a read length of 2 × 100 bp to a target depth of 30 million
487 reads per sample.
488

489 ***RNA sequencing analysis.*** For RNAseq-data processing and alignment, raw sequencing data were
490 processed using the bcl2fastq software (Illumina) to demultiplex and convert base call files into
491 FASTQ format. Quality control of the FASTQ files was performed using FastQC (v0.11.9) to
492 assess read quality, adapter content, and GC distribution. Low-quality reads and adapter sequences
493 were trimmed using Trimmomatic (v0.39). Cleaned reads were aligned to the mouse reference
494 genome (GRCm39) using STAR (v2.7.10a) with default parameters, generating BAM files for
495 each sample. For the differential gene expression, Gene expression quantification was performed
496 using featureCounts (v2.0.3) to obtain raw read counts per gene, based on the GENCODE M28
497 annotation. Count data were provided in a tab-delimited file containing unique read counts for
498 each gene across samples. The dataset was preprocessed using R (R Core Team, 2023). Gene count
499 matrices were normalized using the DESeq2 package (66), which applies a variance-stabilizing
500 transformation to adjust for sequencing depth and RNA composition biases. Differential gene
501 expression analyses were performed using DESeq2's generalized linear model framework,
502 considering the experimental condition as the primary variable. To identify the top differentially
503 expressed genes, the normalized counts were z-score transformed. Heatmaps of the top 20
504 differentially expressed genes were generated using the pheatmap package (67), with sample group
505 annotations included for clarity. Gene identifiers were converted to gene symbols using the
506 org.Mm.eg.db annotation database (68). Pathway enrichment analysis was performed on
507 differentially expressed genes using the Cluster Profiler package (v4.8.1) in R. Gene Ontology
508 (GO) biological processes were analyzed, with pathways considered significant at a false discovery
509 rate < 0.05. The selected resulting pathways were visualized using dot plots generated with ggplot2
510 (v3.4.0).
511
512 ***Bacterial DNA extraction.*** Fecal samples were collected directly from the bedding-free cage floor
513 to avoid contamination. Immediately after collection, fecal samples were frozen at −80 °C until
514 further processing. Bacterial DNA from feces was extracted using the Purelink^{TM} Microbiome
515 DNA Purification Kit (Thermo Fisher Scientific), according to the manufacturer instructions. The
516 concentration and purity of extracted DNA were assessed with a NanoDrop spectrophotometer
517 (Thermo Fisher Scientific).
518

519 ***16S ribosome RNA gene amplification, and sequencing.*** For the amplification of the 16S rRNA
520 gene, primers targeting the V3-V4 hypervariable regions were designed to cover the bacterial
521 domain (84.2%), archaea (75.8%), based on the SILVA database (March 2020). PCR reactions
522 were performed using 10 ng of DNA as input, combining targeted amplification with barcode
523 addition for sample multiplexing. The resulting amplicons were approximately 606 base pairs in
524 length. The amplification process utilized the Quick-16S Plus NGS Library Prep Kit (Zymo
525 Research) according to the manufacturer's instructions. Following amplification, libraries were
526 pooled in equimolar volumes and purified using magnetic beads to remove residual primers and
527 small fragments, as specified by the kit's protocol. Sequencing of the libraries was performed on
528 the NextSeq 2000 platform (Illumina, San Diego, CA) using a paired-end (2x300 bp) approach.
529 This setup ensured high-resolution reads suitable for downstream taxonomic and functional
530 analyses. A minimum of 50,000 reads per sample was targeted to achieve sufficient depth for
531 robust microbial community profiling.
532
533 ***Metagenomic analysis.*** The raw data was first quality controlled by trimming low-quality bases
534 and removing adapters using Trimmomatic. Next, the sequences were denoised and chimeras were
535 removed using the DADA2 algorithm implemented in QIIME 2. Following denoising, the
536 sequences were assigned taxonomy at the genus level using the SILVA v138 database and a Naïve
537 Bayes classifier, which classifies each ASV based on its sequence similarity to known reference
538 sequences. Phyloseq package was used to create a phyloseq object from the ASV table, taxonomic
539 classification, and metadata. The data was then aggregated at the genus level using the tax_glom()
540 function, and relative abundances were calculated using the transform_sample_counts() function
541 in the phyloseq package. The entire workflow was performed using the phyloseq, ggplot2, dplyr,
542 and writexl R packages (69,70).
543
544 ***Statistical analysis.*** For two variables analysis, normality tests Shapiro-Wilk and Kolmogorov-
545 Smirnov were used to elucidate parametric and non-parametric groups. Where at least, one of the
546 independent groups was not following normality, non-parametric analysis was used. For testing
547 differences between two independent groups, Mann-Whitney test was used for non-parametric
548 data, and student *t*-test was used for parametric data. one-way ANOVA test was used for
549 parametric data. For three or more variables analysis, two-way ANOVA test was used. Between

each ANOVA test, multivariant test analysis was used to compare each bidirectional comparison between single groups (Holm-Sidak's test for the parametric one-way ANOVA multivariant analysis, Sidak´s test for two-way ANOVA multivariant analysis). For correlations, non-parametric Spearman test was used. Outliers were discarded when were significant for the Grubb's test.

557 **Disclosure Statement and conflict of interest**

558 PP and JJMG declare that they are inventors in a patent filed on March 2020 by the Fundación
559 para la Formación e Investigación Sanitaria de la Región de Murcia (PCT/EP2020/056729) for a
560 method to identify NLRP3-immunocompromised septic patients. PP, JJM-G, LH-N and AB-M are
561 co-founders of Viva in vitro diagnostics SL, but declare that the research was conducted in the
562 absence of any commercial or financial relationships that could be construed as a potential conflict
563 of interest. The remaining authors declare no competing interests.

564

565 **Funding**

566 This work was supported by grants from MCIN/AEI/10.13039/501100011033 and European
567 Union «Next Generation EU/PRTR» (grants PID2020-116709RB-I00, CNS2022-135105,
568 PID2023-147531OB-I00 and RED2022-134511-T to PP), the Instituto Salud Carlos III co-
569 founded by the European Union (grants AC22/00009 to PP, and PI24/00129 to AB-M) and the
570 Fundación Séneca (grants 21897/PI/22 to PP and 21967/JLI/22 to JJM-G). JJM-G was supported
571 by the Maria Zambrano and Ramon y Cajal fellowships at University of Murcia. AG was supported
572 by an FPI doctoral fellowship from *Ministerio de Ciencia, Innovación y Universidades* (PRE2021-
573 100356). SVM was funded by a predoctoral grant from Instituto de Salud Carlos III co-funded by
574 the European Union (FI21/00073). CM-L was funded by the fellowship PRE2018-086824
575 (Ministerio economía y competitividad). LH-N was supported by the fellowship 21214/FPI/19
576 (Fundación Séneca, Spain).

577

578 **Acknowledgements**

579 We thank AI Gomez for cell culture and lab assistance, and the members of Dr. Pelegrin's
580 laboratory for all comments and suggestions. We also acknowledge to the animal facility and cell
581 culture facility from the University of Murcia, as well as the SPF-animal house, Pathology,
582 Genomics and Bioinformatics platforms from the Pascual Parrilla-Biomedical Research Institute
583 of Murcia (IMIB).

584

585 **Authors Contribution**

586 JJM-G visualized and administered the research. JJM-G and PP conceptualized, supervised,
587 provided funding, and wrote the manuscript. JJM-G and SR did the formal analysis, wrote, and

edited the manuscript. AB-M provided funding and supervision. JJM-G, AG, IQ-R, SV-M. CM-L and LH-N performed the experimental research.

590 **REFERENCES**

591 1. Medzhitov R. Origin and physiological roles of inflammation. *Nature* (2008) 454:428–435. doi:
592 10.1038/nature07201
593 2. Sharma D, Kanneganti T-D. The cell biology of inflammasomes: Mechanisms of inflammasome activation
594 and regulation. *Journal of Cell Biology* (2016) 213:617–629. doi: 10.1083/jcb.201602089
595 3. Tartey S, Kanneganti T. Differential role of the NLRP3 inflammasome in infection and tumorigenesis.
596 *Immunology* (2019) 156:329–338. doi: 10.1111/imm.13046
597 4. Akira S, Uematsu S, Takeuchi O. Pathogen Recognition and Innate Immunity. *Cell* (2006) 124:783–801.
598 doi: 10.1016/j.cell.2006.02.015
599 5. Martinon F, Burns K, Tschopp J. The Inflammasome: a molecular platform triggering activation of
600 inflammatory caspases and processing of proIL-beta. *Mol Cell* (2002) 10:417–426. doi: 10.1016/S1097-
601 2765(02)00599-3
602 6. Shi J, Zhao Y, Wang K, Shi X, Wang Y, Huang H, Zhuang Y, Cai T, Wang F, Shao F. Cleavage of
603 GSDMD by inflammatory caspases determines pyroptotic cell death. *Nature* (2015) 526:660–665. doi:
604 10.1038/nature15514
605 7. Kayagaki N, Kornfeld OS, Lee BL, Stowe IB, O'Rourke K, Li Q, Sandoval W, Yan D, Kang J, Xu M, et al.
606 NINJ1 mediates plasma membrane rupture during lytic cell death. *Nature* (2021) 591:131–136. doi:
607 10.1038/s41586-021-03218-7
608 8. Baroja-Mazo A, Martín-Sánchez F, Gomez AI, Martínez CM, Amores-Iniesta J, Compan V, Barberà-
609 Cremades M, Yagüe J, Ruiz-Ortiz E, Antón J, et al. The NLRP3 inflammasome is released as a particulate
610 danger signal that amplifies the inflammatory response. *Nat Immunol* (2014) 15:738–748. doi:
611 10.1038/ni.2919
612 9. Franklin BS, Bossaller L, De Nardo D, Ratter JM, Stutz A, Engels G, Brenker C, Nordhoff M, Mirandola
613 SR, Al-Amoudi A, et al. The adaptor ASC has extracellular and "prionoid" activities that propagate
614 inflammation. *Nat Immunol* (2014) 15:727–737. doi: 10.1038/ni.2913
615 10. Losa M, Emmenegger M, De Rossi P, Schürch PM, Serdiuk T, Pengo N, Capron D, Bieli D, Bargenda N,
616 Rupp NJ, et al. The ASC inflammasome adapter governs SAA-derived protein aggregation in inflammatory
617 amyloidosis. *EMBO Mol Med* (2024) 16:2024–2042. doi: 10.1038/s44321-024-00107-0
618 11. Alarcón-Vila C, Hurtado-Navarro L, Mateo S V, Peñín-Franch A, Martínez CM, Molina-López C, Baños
619 MC, Gómez AI, Gómez-Román J, Baroja-Mazo A, et al. The inflammasome adaptor protein ASC promotes
620 amyloid deposition in cryopyrin-associated periodic syndromes. *EMBO Mol Med* (2024) 17:41–53. doi:
621 10.1038/s44321-024-00176-1
622 12. Bertheloot D, Wanderley CW, Schneider AH, Schiffelers LD, Wuerth JD, Tödtmann JM, Maasewerd S,
623 Hawwari I, Duthie F, Rohland C, et al. Nanobodies dismantle post-pyroptotic ASC specks and counteract
624 inflammation *in vivo*. *EMBO Mol Med* (2022) 14: doi: 10.15252/emmm.202115415
625 13. Venegas C, Kumar S, Franklin BS, Dierkes T, Brinkschulte R, Tejera D, Vieira-Saecker A, Schwartz S,
626 Santarelli F, Kummer MP, et al. Microglia-derived ASC specks cross-seed amyloid-β in Alzheimer's
627 disease. *Nature* (2017) 552:355–361. doi: 10.1038/nature25158
628 14. Henry LP, Bruijning M, Forsberg SKG, Ayroles JF. The microbiome extends host evolutionary potential.
629 *Nat Commun* (2021) 12:5141. doi: 10.1038/s41467-021-25315-x
630 15. Kudelka MR, Stowell SR, Cummings RD, Neish AS. Intestinal epithelial glycosylation in homeostasis and
631 gut microbiota interactions in IBD. *Nat Rev Gastroenterol Hepatol* (2020) 17:597–617. doi:
632 10.1038/s41575-020-0331-7
633 16. Muller PA, Matheis F, Schneeberger M, Kerner Z, Jové V, Mucida D. Microbiota-modulated CART+
634 enteric neurons autonomously regulate blood glucose. *Science (1979)* (2020) 370:314–321. doi:
635 10.1126/science.abd6176
636 17. Seo S-U, Kamada N, Muñoz-Planillo R, Kim Y-G, Kim D, Koizumi Y, Hasegawa M, Himpsl SD, Browne
637 HP, Lawley TD, et al. Distinct Commensals Induce Interleukin-1β via NLRP3 Inflammasome in
638 Inflammatory Monocytes to Promote Intestinal Inflammation in Response to Injury. *Immunity* (2015)
639 42:744–755. doi: 10.1016/j.immuni.2015.03.004
640 18. Feng Y, Huang Y, Wang Y, Wang P, Song H, Wang F. Antibiotics induced intestinal tight junction barrier
641 dysfunction is associated with microbiota dysbiosis, activated NLRP3 inflammasome and autophagy. *PLoS*
642 *One* (2019) 14:e0218384. doi: 10.1371/journal.pone.0218384
643 19. Sokolova M, Yang K, Hansen SH, Louwe MC, Kummen M, Hov JER, Sjaastad I, Berge RK, Halvorsen B,
644 Aukrust P, et al. NLRP3 inflammasome deficiency attenuates metabolic disturbances involving alterations

in the gut microbial profile in mice exposed to high fat diet. *Sci Rep* (2020) 10:21006. doi: 10.1038/s41598-020-76497-1

20. Finucane OM, Lyons CL, Murphy AM, Reynolds CM, Klinger R, Healy NP, Cooke AA, Coll RC, McAllan L, Nilaweera KN, et al. Monounsaturated Fatty Acid–Enriched High-Fat Diets Impede Adipose NLRP3 Inflammasome–Mediated IL-1β Secretion and Insulin Resistance Despite Obesity. *Diabetes* (2015) 64:2116–2128. doi: 10.2337/db14-1098
21. Levy M, Thaiss CA, Zeevi D, Dohnalová L, Zilberman-Schapira G, Mahdi JA, David E, Savidor A, Korem T, Herzig Y, et al. Microbiota-Modulated Metabolites Shape the Intestinal Microenvironment by Regulating NLRP6 Inflammasome Signaling. *Cell* (2015) 163:1428–1443. doi: 10.1016/j.cell.2015.10.048
22. Zhang J, Yu Q, Jiang D, Yu K, Yu W, Chi Z, Chen S, Li M, Yang D, Wang Z, et al. Epithelial Gasdermin D shapes the host-microbial interface by driving mucus layer formation. *Sci Immunol* (2022) 7: doi: 10.1126/sciimmunol.abk2092
23. Miao P, Ruiqing T, Yanrong L, Zhuwen S, Huan Y, Qiong W, Yongnian L, Chao S. Pyroptosis: A possible link between obesity-related inflammation and inflammatory diseases. *J Cell Physiol* (2022) 237:1245–1265. doi: 10.1002/jcp.30627
24. Opoku E, Traughber CA, Zhang D, Iacano AJ, Khan M, Han J, Smith JD, Gulshan K. Gasdermin D Mediates Inflammation-Induced Defects in Reverse Cholesterol Transport and Promotes Atherosclerosis. *Front Cell Dev Biol* (2021) 9: doi: 10.3389/fcell.2021.715211
25. Xu B, Jiang M, Chu Y, Wang W, Chen D, Li X, Zhang Z, Zhang D, Fan D, Nie Y, et al. Gasdermin D plays a key role as a pyroptosis executor of non-alcoholic steatohepatitis in humans and mice. *J Hepatol* (2018) 68:773–782. doi: 10.1016/j.jhep.2017.11.040
26. Ahmad F, Mishra N, Ahrenstorf G, Franklin BS, Latz E, Schmidt RE, Bossaller L. Evidence of inflammasome activation and formation of monocyte-derived ASC specks in HIV-1 positive patients. *AIDS* (2018) 32:299–307. doi: 10.1097/QAD.0000000000001693
27. Elinav E, Strowig T, Kau AL, Henao-Mejia J, Thaiss CA, Booth CJ, Peaper DR, Bertin J, Eisenbarth SC, Gordon JI, et al. NLRP6 inflammasome regulates colonic microbial ecology and risk for colitis. *Cell* (2011) 145:745–57. doi: 10.1016/j.cell.2011.04.022
28. Mamantopoulos M, Ronchi F, Van Hauwermeiren F, Vieira-Silva S, Yilmaz B, Martens L, Saeys Y, Drexler SK, Yazdi AS, Raes J, et al. Nlrp6- and ASC-Dependent Inflammasomes Do Not Shape the Commensal Gut Microbiota Composition. *Immunity* (2017) 47:339-348.e4. doi: 10.1016/j.immuni.2017.07.011
29. Alfieri M, Pomerleau J, Grace DM. A comparison of fat intake of normal weight, moderately obese and severely obese subjects. *Obes Surg* (1997) 7:9–15. doi: 10.1381/096089297765556150
30. Raatz SK, Conrad Z, Johnson LK, Picklo MJ, Jahns L. Relationship of the Reported Intakes of Fat and Fatty Acids to Body Weight in US Adults. *Nutrients* (2017) 9: doi: 10.3390/nu9050438
31. Markovich Z, Abreu A, Sheng Y, Han SM, Xiao R. Deciphering internal and external factors influencing intestinal junctional complexes. *Gut Microbes* (2024) 16: doi: 10.1080/19490976.2024.2389320
32. Greer RL, Dong X, Moraes ACF, Zielke RA, Fernandes GR, Peremyslova E, Vasquez-Perez S, Schoenborn AA, Gomes EP, Pereira AC, et al. Akkermansia muciniphila mediates negative effects of IFNγ on glucose metabolism. *Nat Commun* (2016) 7:13329. doi: 10.1038/ncomms13329
33. Geach T. Mucin-munching bacteria modulate glucose metabolism. *Nat Rev Endocrinol* (2017) 13:66–66. doi: 10.1038/nrendo.2016.201
34. Matsumoto H, Shiotani A, Katsumata R, Fukushima S, Handa Y, Osawa M, Murao T, Handa O, Umegaki E, Inoue R, et al. Mucosa-Associated Microbiota in Patients with Irritable Bowel Syndrome: A Comparison of Subtypes. *Digestion* (2021) 102:49–56. doi: 10.1159/000512167
35. Sugihara K, Kitamoto S, Saraithong P, Nagao-Kitamoto H, Hoostal M, McCarthy C, Rosevelt A, Muraleedharan CK, Gillilland MG, Imai J, et al. Mucolytic bacteria license pathobionts to acquire host-derived nutrients during dietary nutrient restriction. *Cell Rep* (2022) 40:111093. doi: 10.1016/j.celrep.2022.111093
36. Companys J, Gosalbes MJ, Pla-Pagà L, Calderón-Pérez L, Llauradó E, Pedret A, Valls RM, Jiménez-Hernández N, Sandoval-Ramirez BA, Del Bas JM, et al. Gut Microbiota Profile and Its Association with Clinical Variables and Dietary Intake in Overweight/Obese and Lean Subjects: A Cross-Sectional Study. *Nutrients* (2021) 13: doi: 10.3390/nu13062032
37. Tanaka T, Fujii T, Takahashi H, Kuramitsu K, Funasaka K, Ohno E, Akimoto S, Nakauchi M, Shibasaki S, Uyama I, et al. Association between Microbiome Dysbiosis and Postoperative Disorders before and after Gastrectomy. *Digestion* (2025)1–13. doi: 10.1159/000545678

38. McMullen BN, Chen See J, Baker S, Wright JR, Anderson SLC, Yochum G, Koltun W, Portolese A, Jeganathan NA, Lamendella R. Metatranscriptomic analysis of colonic mucosal samples exploring the functional role of active microbial consortia in complicated diverticulitis. *Microbiol Spectr* (2025)e0243124. doi: 10.1128/spectrum.02431-24
39. Mbaye B, Magdy Wasfy R, Borentain P, Tidjani Alou M, Mottola G, Bossi V, Caputo A, Gerolami R, Million M. Increased fecal ethanol and enriched ethanol-producing gut bacteria Limosilactobacillus fermentum, Enterocloster bolteae, Mediterraneibacter gnavus and Streptococcus mutans in nonalcoholic steatohepatitis. *Front Cell Infect Microbiol* (2023) 13:1279354. doi: 10.3389/fcimb.2023.1279354
40. Brooks JF, Behrendt CL, Ruhn KA, Lee S, Raj P, Takahashi JS, Hooper L V. The microbiota coordinates diurnal rhythms in innate immunity with the circadian clock. *Cell* (2021) 184:4154-4167.e12. doi: 10.1016/j.cell.2021.07.001
41. Huber-Ruano I, Calvo E, Mayneris-Perxachs J, Rodríguez-Peña M-M, Ceperuelo-Mallafré V, Cedó L, Núñez-Roa C, Miro-Blanch J, Arnoriaga-Rodríguez M, Balvay A, et al. Orally administered Odoribacter laneus improves glucose control and inflammatory profile in obese mice by depleting circulating succinate. *Microbiome* (2022) 10:135. doi: 10.1186/s40168-022-01306-y
42. Yao Y, Kim G, Shafer S, Chen Z, Kubo S, Ji Y, Luo J, Yang W, Perner SP, Kanellopoulou C, et al. Mucus sialylation determines intestinal host-commensal homeostasis. *Cell* (2022) 185:1172-1188.e28. doi: 10.1016/j.cell.2022.02.013
43. Taniguchi M, Okumura R, Matsuzaki T, Nakatani A, Sakaki K, Okamoto S, Ishibashi A, Tani H, Horikiri M, Kobayashi N, et al. Sialylation shapes mucus architecture inhibiting bacterial invasion in the colon. *Mucosal Immunol* (2023) 16:624–641. doi: 10.1016/j.mucimm.2023.06.004
44. Yu K, Li Q, Sun X, Peng X, Tang Q, Chu H, Zhou L, Wang B, Zhou Z, Deng X, et al. Bacterial indole-3-lactic acid affects epithelium–macrophage crosstalk to regulate intestinal homeostasis. *Proceedings of the National Academy of Sciences* (2023) 120: doi: 10.1073/pnas.2309032120
45. Tirado-Hurtado I, Fajardo W, Pinto JA. DNA Damage Inducible Transcript 4 Gene: The Switch of the Metabolism as Potential Target in Cancer. *Front Oncol* (2018) 8: doi: 10.3389/fonc.2018.00106
46. Merino B, Fernández-Díaz CM, Parrado-Fernández C, González-Casimiro CM, Postigo-Casado T, Lobatón CD, Leissring MA, Cózar-Castellano I, Perdomo G. Hepatic insulin-degrading enzyme regulates glucose and insulin homeostasis in diet-induced obese mice. *Metabolism* (2020) 113:154352. doi: 10.1016/j.metabol.2020.154352
47. Su Q, Huang J, Chen X, Wang Y, Shao M, Yan H, Chen C, Ren H, Zhang F, Ni Y, et al. Long-Term High-Fat Diet Decreases Renal Insulin-Degrading Enzyme Expression and Function by Inhibiting the PPARγ Pathway. *Mol Nutr Food Res* (2023) 67: doi: 10.1002/mnfr.202200589
48. Bauer C, Duewell P, Mayer C, Lehr HA, Fitzgerald KA, Dauer M, Tschopp J, Endres S, Latz E, Schnurr M. Colitis induced in mice with dextran sulfate sodium (DSS) is mediated by the NLRP3 inflammasome. *Gut* (2010) 59:1192–1199. doi: 10.1136/gut.2009.197822
49. Frühbeck G, Gómez-Ambrosi J, Ramírez B, Becerril S, Rodríguez A, Mentxaka A, Valentí V, Moncada R, Reina G, Baixauli J, et al. Decreased expression of the NLRP6 inflammasome is associated with increased intestinal permeability and inflammation in obesity with type 2 diabetes. *Cellular and Molecular Life Sciences* (2024) 81:77. doi: 10.1007/s00018-024-05124-3
50. Tye H, Yu C-H, Simms LA, de Zoete MR, Kim ML, Zakrzewski M, Penington JS, Harapas CR, Souza-Fonseca-Guimaraes F, Wockner LF, et al. NLRP1 restricts butyrate producing commensals to exacerbate inflammatory bowel disease. *Nat Commun* (2018) 9:3728. doi: 10.1038/s41467-018-06125-0
51. Mullins B, Chen J. NLRP9 in innate immunity and inflammation. *Immunology* (2021) 162:262–267. doi: 10.1111/imm.13290
52. Eckel RH, Grundy SM, Zimmet PZ. The metabolic syndrome. *The Lancet* (2005) 365:1415–1428. doi: 10.1016/S0140-6736(05)66378-7
53. Hamblin PS, Russell AW, Talic S, Zoungas S. The growing range of complications of diabetes mellitus. *Trends in Endocrinology & Metabolism* (2025) doi: 10.1016/j.tem.2024.12.006
54. Honda M, Kadohisa M, Yoshii D, Komohara Y, Hibi T. Directly recruited GATA6 + peritoneal cavity macrophages contribute to the repair of intestinal serosal injury. *Nat Commun* (2021) 12:7294. doi: 10.1038/s41467-021-27614-9
55. Cyr B, Vontell RT, Hadad R, de Rivero Vaccari JP, Keane RW. IC100 blocks inflammasome activation induced by α-synuclein aggregates and ASC specks. *NPJ Parkinsons Dis* (2025) 11:92. doi: 10.1038/s41531-025-00963-8

755 56. Yuan H, Chen S, Duncan MR, de Rivero Vaccari JP, Keane RW, Dalton Dietrich W, Chou T-H, Benny M,
756 Schmidt AF, Young K, et al. IC100, a humanized therapeutic monoclonal anti-ASC antibody alleviates
757 oxygen-induced retinopathy in mice. *Angiogenesis* (2024) 27:423–440. doi: 10.1007/s10456-024-09917-9
758 57. Desu HL, Plastini M, Illiano P, Bramlett HM, Dietrich WD, de Rivero Vaccari JP, Brambilla R, Keane RW.
759 IC100: a novel anti-ASC monoclonal antibody improves functional outcomes in an animal model of
760 multiple sclerosis. *J Neuroinflammation* (2020) 17:143. doi: 10.1186/s12974-020-01826-0
761 58. Soriano-Teruel PM, García-Laínez G, Marco-Salvador M, Pardo J, Arias M, DeFord C, Merfort I, Vicent
762 MJ, Pelegrín P, Sancho M, et al. Identification of an ASC oligomerization inhibitor for the treatment of
763 inflammatory diseases. *Cell Death Dis* (2021) 12:1155. doi: 10.1038/s41419-021-04420-1
764 59. García-Fernández A, Sancho M, Garrido E, Bisbal V, Sancenón F, Martínez-Máñez R, Orzáez M. Targeted
765 Delivery of the Pan-Inflammasome Inhibitor MM01 as an Alternative Approach to Acute Lung Injury
766 Therapy. *Adv Healthc Mater* (2023) 12:e2301577. doi: 10.1002/adhm.202301577
767 60. de Paula Souza J, Fischer JS, Jeanneau K, Allard C, Angevaare E, Aschenbrenner D, Bodendorf U,
768 Demarco B, Gounarides JS, Killmer S, et al. Blood characteristics of patients with type 2 diabetes and
769 response of their peripheral blood mononuclear cells to inhibitors of the NLRP3-inflammasome and
770 caspase-1. *Can J Diabetes* (2025) doi: 10.1016/j.jcjd.2025.06.008
771 61. Villalva M, Martínez-García JJ, Jaime L, Santoyo S, Pelegrín P, Pérez-Jiménez J. Polyphenols as NLRP3
772 inflammasome modulators in cardiometabolic diseases: a review of in vivo studies. *Food Funct* (2023)
773 14:9534–9553. doi: 10.1039/d3fo03015f
774 62. Huang C, Liu Q, Tang Q, Jing X, Wu T, Zhang J, Zhang G, Zhou J, Zhang Z, Zhao Y, et al. Hepatocyte-
775 specific deletion of Nlrp6 in mice exacerbates the development of non-alcoholic steatohepatitis. *Free Radic*
776 *Biol Med* (2021) 169:110–121. doi: 10.1016/j.freeradbiomed.2021.04.008
777 63. Coll RC, Schroder K, Pelegrín P. NLRP3 and pyroptosis blockers for treating inflammatory diseases. *Trends*
778 *Pharmacol Sci* (2022) 43:653–668. doi: 10.1016/j.tips.2022.04.003
779 64. Pelegrín P. Targeting Interleukin-1 Signaling in Chronic Inflammation: Focus on P2X7 Receptor and
780 Pannexin-1. *Drug News Perspect* (2008) 21:424. doi: 10.1358/dnp.2008.21.8.1265800
781 65. Sunny NE, Bril F, Cusi K. Mitochondrial Adaptation in Nonalcoholic Fatty Liver Disease: Novel
782 Mechanisms and Treatment Strategies. *Trends in Endocrinology & Metabolism* (2017) 28:250–260. doi:
783 10.1016/j.tem.2016.11.006
784 66. Love MI, Huber W, Anders S. Moderated estimation of fold change and dispersion for RNA-seq data with
785 DESeq2. *Genome Biol* (2014) 15:550. doi: 10.1186/s13059-014-0550-8
786 67. Kolde R. pheatmap: Pretty Heatmaps. *CRAN: Contributed Packages* (2019) doi:
787 10.32614/CRAN.package.pheatmap
788 68. Carlson M. Genome wide annotation for Mouse, primarily based on mapping using Entrez Gene identifiers.
789 *Bioconductor Package Maintainer* (2023)
790 69. Wickham H. *ggplot2: Elegant Graphics for Data Analysis.* 2nd edition. Springer. (2016).
791 70. McMurdie PJ, Holmes S. phyloseq: An R Package for Reproducible Interactive Analysis and Graphics of
792 Microbiome Census Data. *PLoS One* (2013) 8:e61217. doi: 10.1371/journal.pone.0061217
793 71. Mariathasan S, Newton K, Monack DM, Vucic D, French DM, Lee WP, Roose-Girma M, Erickson S, Dixit
794 VM. Differential activation of the inflammasome by caspase-1 adaptors ASC and Ipaf. *Nature* (2004)
795 430:213–8. doi: 10.1038/nature02664
796 72. Martínez-García JJ, Martínez-Banaclocha H, Angosto-Bazarra D, de Torre-Minguela C, Baroja-Mazo A,
797 Alarcón-Vila C, Martínez-Alarcón L, Amores-Iniesta J, Martín-Sánchez F, Ercole GA, et al. P2X7 receptor
798 induces mitochondrial failure in monocytes and compromises NLRP3 inflammasome activation during
799 sepsis. *Nat Commun* (2019) 10:2711. doi: 10.1038/s41467-019-10626-x
800 73. Dobin A, Davis CA, Schlesinger F, Drenkow J, Zaleski C, Jha S, Batut P, Chaisson M, Gingeras TR. STAR:
801 ultrafast universal RNA-seq aligner. *Bioinformatics* (2013) 29:15–21. doi: 10.1093/bioinformatics/bts635
802
803

804 **Figure legends**

805 **Figure 1. ASC deficiency prevents glucose intolerance during high fat diet.**

806 **A.** Body weight from wild type (*Pycard*$^{+/+}$, blue, n=5), and *Pycard*$^{-/-}$ (orange, n=4) mice fed with
807 a high fat diet (HFD) for 5 months.

808 **B.** Body weight from *Pycard*$^{+/+}$ (balck, n=3-4), *Pycard*$^{-/-}$ (white, n=2) mice separated by sex, males
809 (discontinuous line) and females (continuous line) fed with a normal chow diet (NCD) for 5
810 months.

811 **C-E.** Glucose tolerance (left) and area under the curve (AUC, right) from mice fed with HFD
812 (C,D) or NCD (E) during 3 months (C,E) or 5 months (D). Wild type (*Pycard*$^{+/+}$, blue, n=5), and
813 *Pycard*$^{-/-}$ (orange, n=4) mice.

814 Bars or dots represent the mean, error bars represent SEM. Two-way ANOVA with multivariant
815 Sidak's test was used for all panels. Mann-Whitney's test was done for C-E. (ns, $p>0.05$, *$p\leq0.05$;
816 **$p\leq0.01$; *** $p\leq0.001$).

817

818 **Figure 2. High fat diet increases intestinal permeability and reduces peritoneal cells**
819 **dependent on ASC.**

820 **A, B**. Number of peritoneal cells (A) and interleukin (IL)-1β release from peritoneal cells (B)
821 treated as indicated in the figure from wild type mice fed for 5 months with a normal chow diet
822 (NCD, n=4, grey) or high fat diet (HFD, n=5, blue).

823 **C, D**. Number of peritoneal cells (C) and IL-1β release from peritoneal cells (D) treated as
824 indicated in the figure from wild type (*Pycard*$^{+/+}$, n=5, blue) or *Pycard*$^{-/-}$ (n=4, orange) mice fed
825 for 5 months with a HFD. LPS: lipopolysaccharide; NIG: nigericin; MCC: MCC950.

826 **E, F.** IL-6 release from peritoneal cells collected from mice treated as in A-D and then *in vitro*
827 stimulated as described in the figure.

828 Each dot in A,C represents a distinct animal, bars represent the mean, error bars represent SEM.
829 Mann-Whitney's test was used for A,C. Two-way ANOVA with multivariant Sidak's test was
830 used for B, D-F (ns, p>0,05; *$p\leq0.05$; **$p\leq0.01$; *** $p\leq0.001$).

831

832 **Figure 3. ASC modulate microbiota biodiversity during high fat diet.**

833 **A-C.** Relative microbiota abundance at level of class (A, B) or families (C) on wild type
834 (*Pycard*$^{+/+}$, n=5) (A, C) or *Pycard*$^{-/-}$ mice (n=4) (B, C) after 5 months of high fat diet (HFD).

835 **D**. Shannon index from the same conditions as in A-C.

836 **E-K**. Relative abundance of *Akkermansia* (E), *Odoribacter* (F), Lachnospiraceae NK4A136 (G),
837 Coriobacteriaceae UGC002 (H), *Lactobacillus* (I), *Streptococcus* (J), and *Dorea* (K) in the same
838 conditions as in A-C.

839 **L.** Intestinal permeability measured by 4 kDa FITC-dextran in *Pycard*$^{+/+}$ NCD (grey, n=4),
840 *Pycard*$^{+/+}$ HFD (blue, n=5), *Pycard*$^{-/-}$ NCD (white, n=4), and *Pycard*$^{-/-}$ HFD (orange, n=4) after 5
841 months of high fat diet (HFD).

842 Each dot represents a distinct animal, bars represent the mean, error bars represent SEM. Mann-
843 Whitney's test was done for D-K. One-way ANOVA with multivariant Holm-Sidak's test was
844 used for L (ns p>0,05; *p≤0.05; **p≤0.01; *** p≤0.001).

845

846 **Figure 4. ASC induces bacteria attachment in small intestinal *villi* during high fat diet.**

847 **A, B.** Haematoxylin and eosin histology of the small intestine of wild type *Pycard*$^{+/+}$ (A) and
848 *Pycard*$^{-/-}$ (B) mice fed for 5 months with a high fat diet (HFD). Scale bar: 200 μm; red arrows
849 denote not attached mucus in the intestinal lumen; black arrows indicate presence of bacteria; blue
850 arrows indicate presence of mucus between *villi*.

851 **C.** *ST6Galnac* gene family transcript expression in the small intestine of mice treated as in A, B.

852 **D**. Interleukin (IL)-1β in the small intestine of mice treated as in A, B. Wild type (*Pycard*$^{+/+}$, n=5,
853 blue), and *Pycard*$^{-/-}$ (n=3, orange) mice.

854 **E**. Differential expressed genes in the small intestine of mice treated as in A, B.

855 **F.** Gene Ontology differential expressed pathways in the small intestine of mice treated as in A,
856 B. Wild type (*Pycard*$^{+/+}$, n=3), and *Pycard*$^{-/-}$ (n=4,) mice.

857 Each dot represents a distinct animal, bars represent the mean, error bars represent SEM. Mann-
858 Whitney's test was used for D (*p≤0.05).

859

860 **Figure 5. ASC deficiency increases glycolytic and mitochondrial metabolism related genes**
861 **during high fat diet.**

862 **A-G.** Relative mRNA expression of *Pkm* (A), *Ldha* (B), *Pdha* (C), *Nnt* (D), *Glud1* (E), *Sdha* (F),
863 and *Cpt1a* (G) on the small intestine of wild type (*Pycard*$^{+/+}$, n=10, red) and *Pycard*$^{-/-}$ (n=4, green)
864 mice fed with HFD for 5 months.

865 Bars represent the mean; error bars represent SEM. Unpaired *t*-test was used (ns, $p>0.05$; *$p\leq0.05$;
866 **$p\leq0.01$).
867
868 **Figure 6. ASC decreases hepatic metabolism and enhances inflammation under high fat diet**
869 **A, B.** Haematoxylin and eosin histology of the liver of wild type (*Pycard*$^{+/+}$, A) and *Pycard*$^{-/-}$ (B)
870 mice fed for 5 months with a high fat diet (HFD). Scale bar: 200 µm; Arrows indicate hepatic
871 vascularization.
872 **C, D.** Interleukin (IL)-1β (C) and IL-6 (D) in the liver of mice treated as in A-B.
873 **E-J.** Relative mRNA expression of *Pgc1a* (E), *Nnt* (F), *Glud1* (G), *Sdha* (H), *Cpt1a* (I) and
874 *Hmgcs2* (J) in the liver of mice treated as in A-B.
875 For C-J, *Pycard*$^{+/+}$ mice (n=10) are represented in blue and *Pycard*$^{-/-}$ mice (n=4) are represented in
876 orange. Each dot in C,D represents a distinct animal, bars represent the mean, error bars represent
877 SEM. Unpaired *t*-test was used for C-J (ns, $p>0.05$; *$p\leq0.05$; *** $p\leq0.001$).
878
879 **Figure 7. Extracellular ASC oligomers partially rescue intestinal microbiota and mucosal**
880 **physiopathology during high fat diet.**
881 **A.** Model representation of the treatment with recombinant ASC oligomers in combination with
882 high fat diet (HFD).
883 **B.** Intestinal permeability measured by 4 kDa FITC-dextran in *Pycard*$^{-/-}$ mice with intraperitoneal
884 injection of recombinant ASC oligomers (+ipASC, orange, n=5) fed for 5 months with a HFD.
885 Wild type (*Pycard*$^{+/+}$, n=4) and *Pycard*$^{-/-}$ (n=4) from Figure 3 are shown in grey for comparison.
886 **C.** Relative abundance of *Odoribacter*, Lachnospiraceae NK4A136, Coriobacteriaceae UGC002,
887 *Lactobacillus*, *Enteractinococcus, Atopostipes, Akkermansia*, *Streptococcus* and *Dorea* in the
888 same conditions as in B.
889 **D, E.** Haematoxylin and eosin histology of the small intestine of *Pycard*$^{-/-}$ mice fed with a HFD
890 for 5 months in the absence (D) or with ipASC (E). Scale bar: 200 µm; blue arrows indicate
891 presence of mucus between *villi* and red arrows indicate not attached mucus.
892 **F.** *ST6Galnac* gene family expression in the small intestine of mice treated as in B.
893 **G.** Relative gene expression of *Nnt, Pkm2*, *Sdha*, *Cpt1a*, *Pdha*, and *Glud1* in the small intestine of
894 mice treated as in B.
895 **H.** Differential expressed genes in the small intestine of mice treated as in B.

896 **I.** Interleukin (IL)-1β in the small intestine of mice treated as in B.

897 **J.** Relative mRNA expression of *Pycard* in the small intestine of mice treated as in B.

898 *Pycard*$^{+/+}$ (n=3-5), *Pycard*$^{-/-}$ (n=3-4), *Pycard*$^{-/-}$ +ipASC (n=3-5).

899 Each dot represents a distinct animal, bars represent the mean, error bars represent SEM. One-way
900 ANOVA with multivariant Holm-Sidak's test was used for B, C, G, I-J (ns, $p>0.05$; *$p\leq0.05$;
901 **$p\leq0.01$; *** $p\leq0.001$).

902

Figure 1

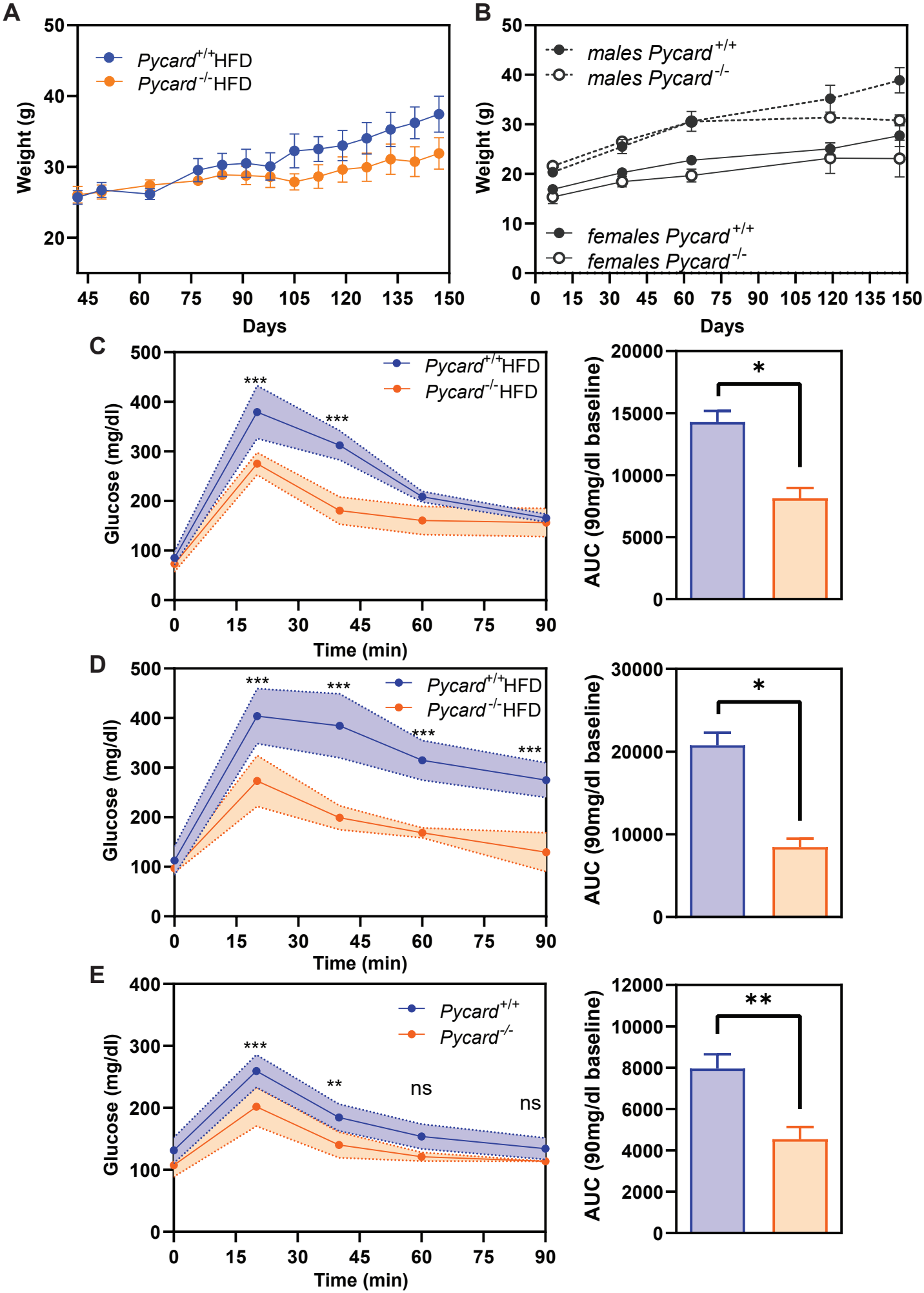
A
Pycard+/+HFD
Pycard-/-HFD
Weight (g)
Days
B
males Pycard+/+
males Pycard-/-
females Pycard+/+
females Pycard-/-
Weight (g)
Days
C
Pycard+/+HFD
Pycard-/-HFD
Glucose (mg/dl)
Time (min)
AUC (90mg/dl baseline)
D
Pycard+/+HFD
Pycard-/-HFD
Glucose (mg/dl)
Time (min)
AUC (90mg/dl baseline)
E
Pycard+/+
Pycard-/-
Glucose (mg/dl)
Time (min)
ns
AUC (90mg/dl baseline)

Figure 2

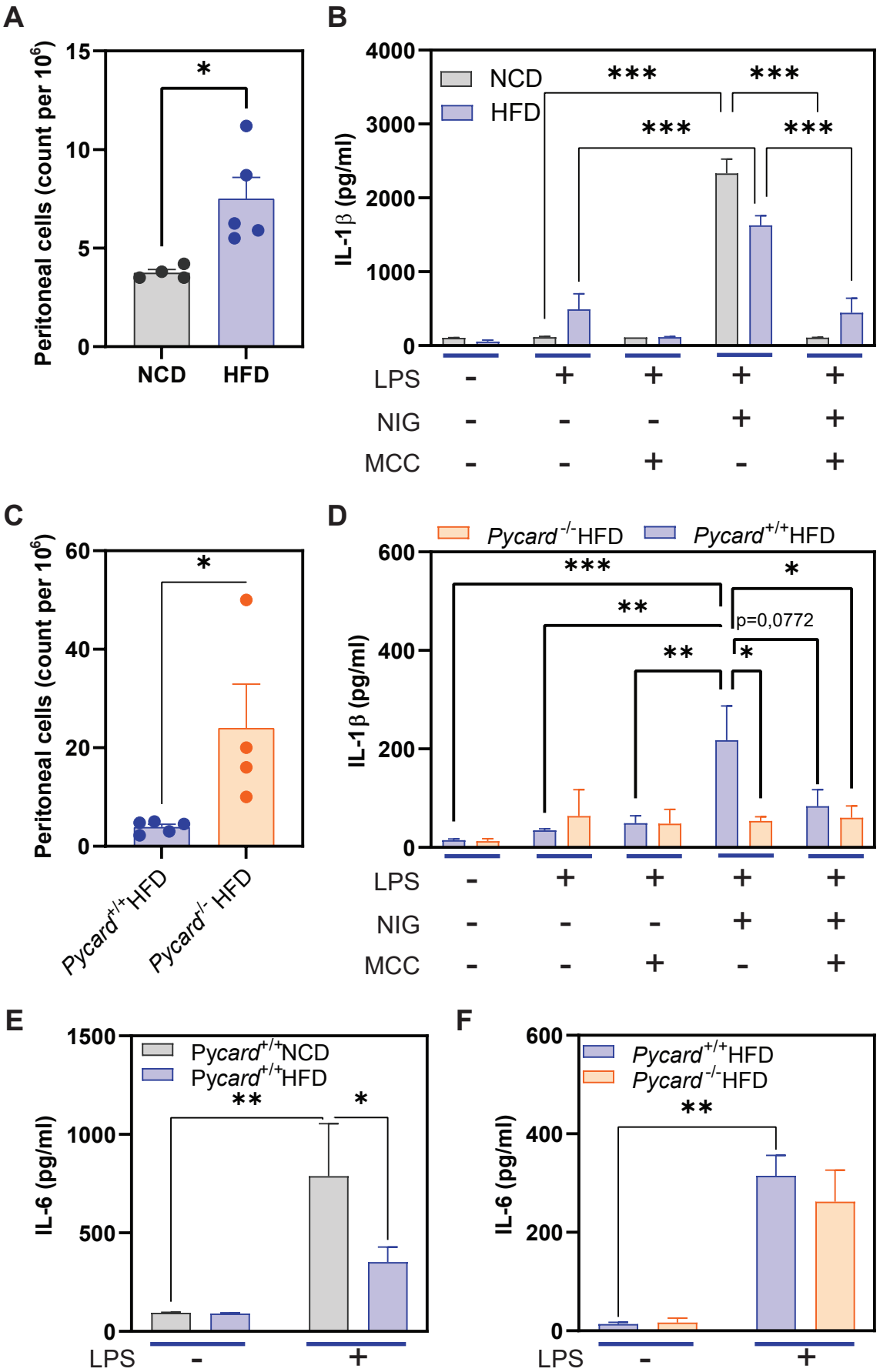
A
Peritoneal cells (count per 10^6)
15
10
5
0
*
NCD
HFD
B
IL-1β (pg/ml)
4000
3000
2000
1000
0
NCD
HFD
***
***
***
***
LPS - + + + +
NIG - - - + +
MCC - - + - +
C
Peritoneal cells (count per 10^6)
60
40
20
0
*
Pycard+/+HFD
Pycard-/- HFD
D
Pycard-/-HFD
Pycard+/+HFD
IL-1β (pg/ml)
600
400
200
0
***
**
**
*
*
p=0,0772
LPS - + + + +
NIG - - - + +
MCC - - + - +
E
IL-6 (pg/ml)
1500
1000
500
0
Pycard+/+NCD
Pycard+/+HFD
**
*
LPS - +
F
IL-6 (pg/ml)
600
400
200
0
Pycard+/+HFD
Pycard-/-HFD
**
LPS - +

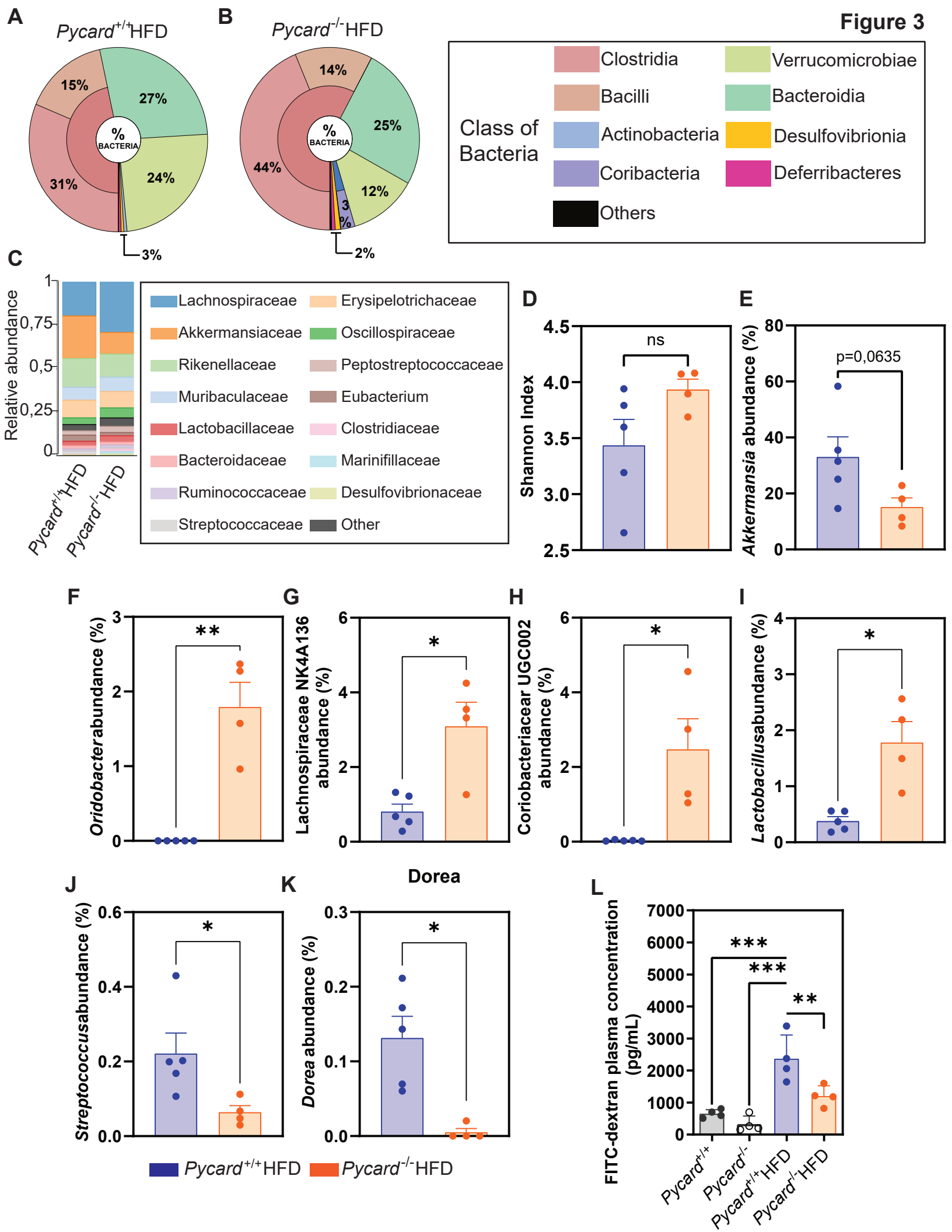
Figure 3
A
Pycard+/+HFD
15%
27%
31%
24%
3%
% BACTERIA
B
Pycard-/-HFD
14%
25%
44%
12%
3%
2%
% BACTERIA
Class of Bacteria
Clostridia
Bacilli
Actinobacteria
Coribacteria
Others
Verrucomicrobiae
Bacteroidia
Desulfovibrionia
Deferribacteres
C
Relative abundance
1
0,75
0,5
0,25
0
Pycard+/+HFD
Pycard-/-HFD
Lachnospiraceae
Akkermansiaceae
Rikenellaceae
Muribaculaceae
Lactobacillaceae
Bacteroidaceae
Ruminococcaceae
Streptococcaceae
Erysipelotrichaceae
Oscillospiraceae
Peptostreptococcaceae
Eubacterium
Clostridiaceae
Marinifillaceae
Desulfovibrionaceae
Other
D
Shannon Index
ns
E
Akkermansia abundance (%)
p=0,0635
F
Oridobacter abundance (%)
**
G
Lachnospiraceae NK4A136 abundance (%)
*
H
Coriobacteriacear UGC002 abundance (%)
*
I
Lactobacillus abundance (%)
*
J
Streptococcus abundance (%)
*
K
Dorea
Dorea abundance (%)
*
L
FITC-dextran plasma concentration (pg/mL)
***
***
**
Pycard+/+
Pycard-/-
Pycard+/+HFD
Pycard-/-HFD
Pycard+/+HFD
Pycard-/-HFD

Figure 4

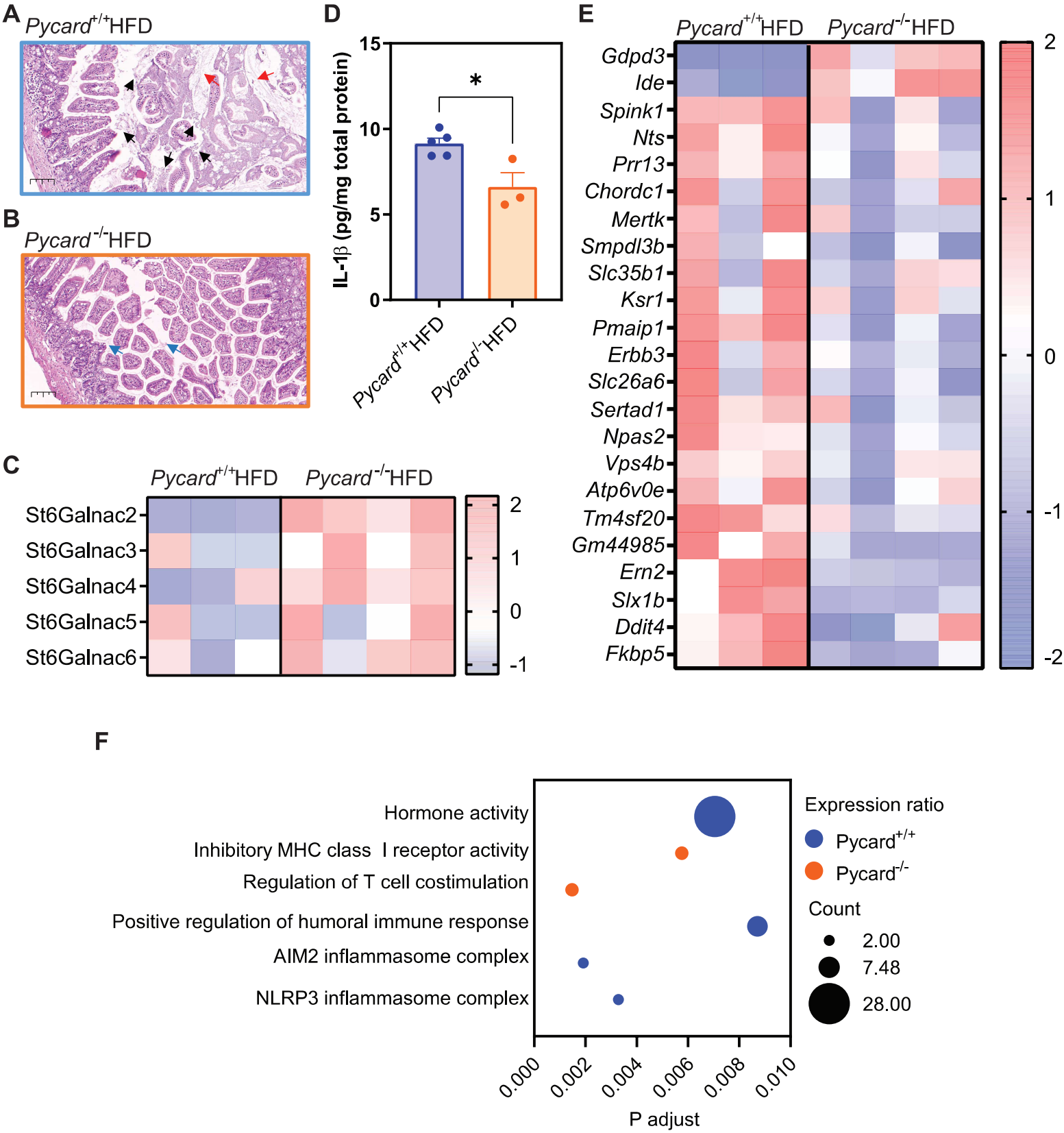
A
Pycard+/+HFD
B
Pycard-/-HFD
D
IL-1β (pg/mg total protein)
15
10
5
0
*
Pycard+/+HFD
Pycard-/-HFD
C
Pycard+/+HFD
Pycard-/-HFD
St6Galnac2
St6Galnac3
St6Galnac4
St6Galnac5
St6Galnac6
2
1
0
-1
E
Pycard+/+HFD
Pycard-/-HFD
Gdpd3
Ide
Spink1
Nts
Prr13
Chordc1
Mertk
Smpdl3b
Slc35b1
Ksr1
Pmaip1
Erbb3
Slc26a6
Sertad1
Npas2
Vps4b
Atp6v0e
Tm4sf20
Gm44985
Ern2
Slx1b
Ddit4
Fkbp5
2
1
0
-1
-2
F
Hormone activity
Inhibitory MHC class I receptor activity
Regulation of T cell costimulation
Positive regulation of humoral immune response
AIM2 inflammasome complex
NLRP3 inflammasome complex
0.000
0.002
0.004
0.006
0.008
0.010
P adjust
Expression ratio
Pycard+/+
Pycard-/-
Count
2.00
7.48
28.00

Figure 5

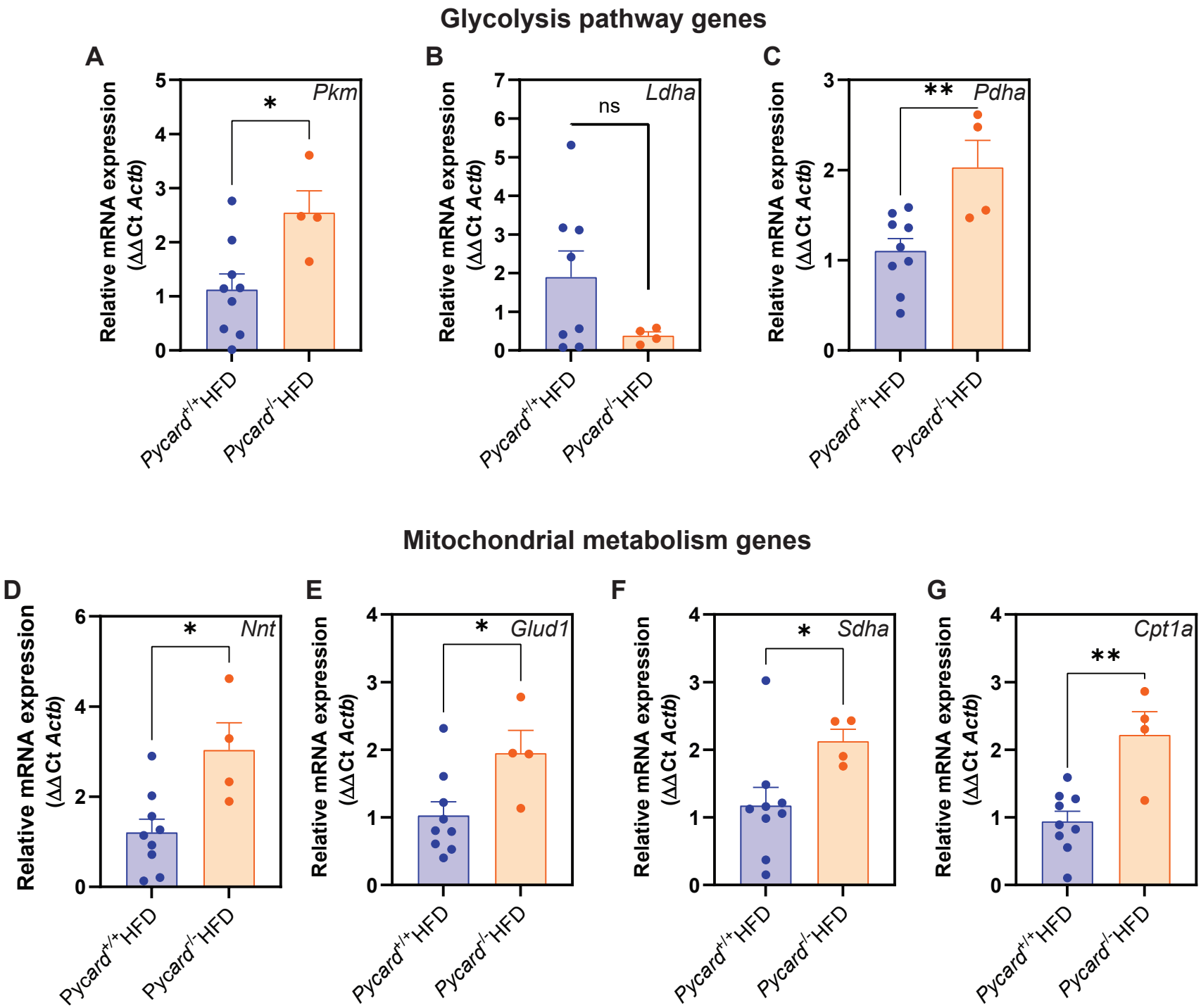
Glycolysis pathway genes
A
Pkm
*
B
Ldha
ns
C
Pdha
**
Relative mRNA expression (ΔΔCt Actb)
Pycard+/+HFD
Pycard-/-HFD
Mitochondrial metabolism genes
D
Nnt
*
E
Glud1
*
F
Sdha
*
G
Cpt1a
**

Figure 6

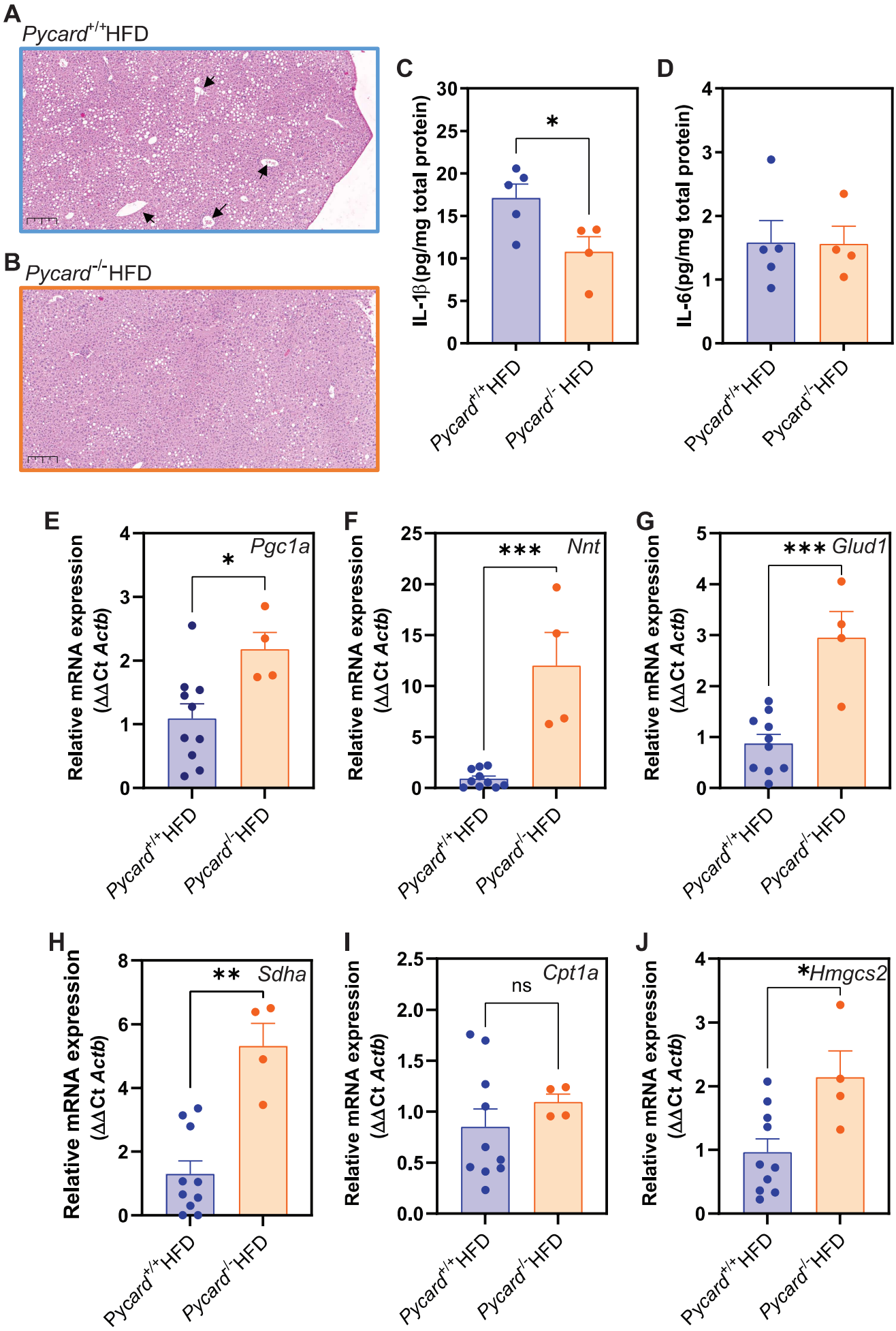
A
Pycard+/+HFD
B
Pycard-/-HFD
C
IL-1β(pg/mg total protein)
*
Pycard+/+HFD
Pycard-/- HFD
D
IL-6(pg/mg total protein)
Pycard+/+HFD
Pycard-/-HFD
E
Relative mRNA expression (ΔΔCt Actb)
Pgc1a
*
Pycard+/+HFD
Pycard-/-HFD
F
Relative mRNA expression (ΔΔCt Actb)
Nnt
***
Pycard+/+HFD
Pycard-/-HFD
G
Relative mRNA expression (ΔΔCt Actb)
*** Glud1
Pycard+/+HFD
Pycard-/-HFD
H
Relative mRNA expression (ΔΔCt Actb)
** Sdha
Pycard+/+HFD
Pycard-/-HFD
I
Relative mRNA expression (ΔΔCt Actb)
Cpt1a
ns
Pycard+/+HFD
Pycard-/-HFD
J
Relative mRNA expression (ΔΔCt Actb)
*Hmgcs2
Pycard+/+HFD
Pycard-/-HFD

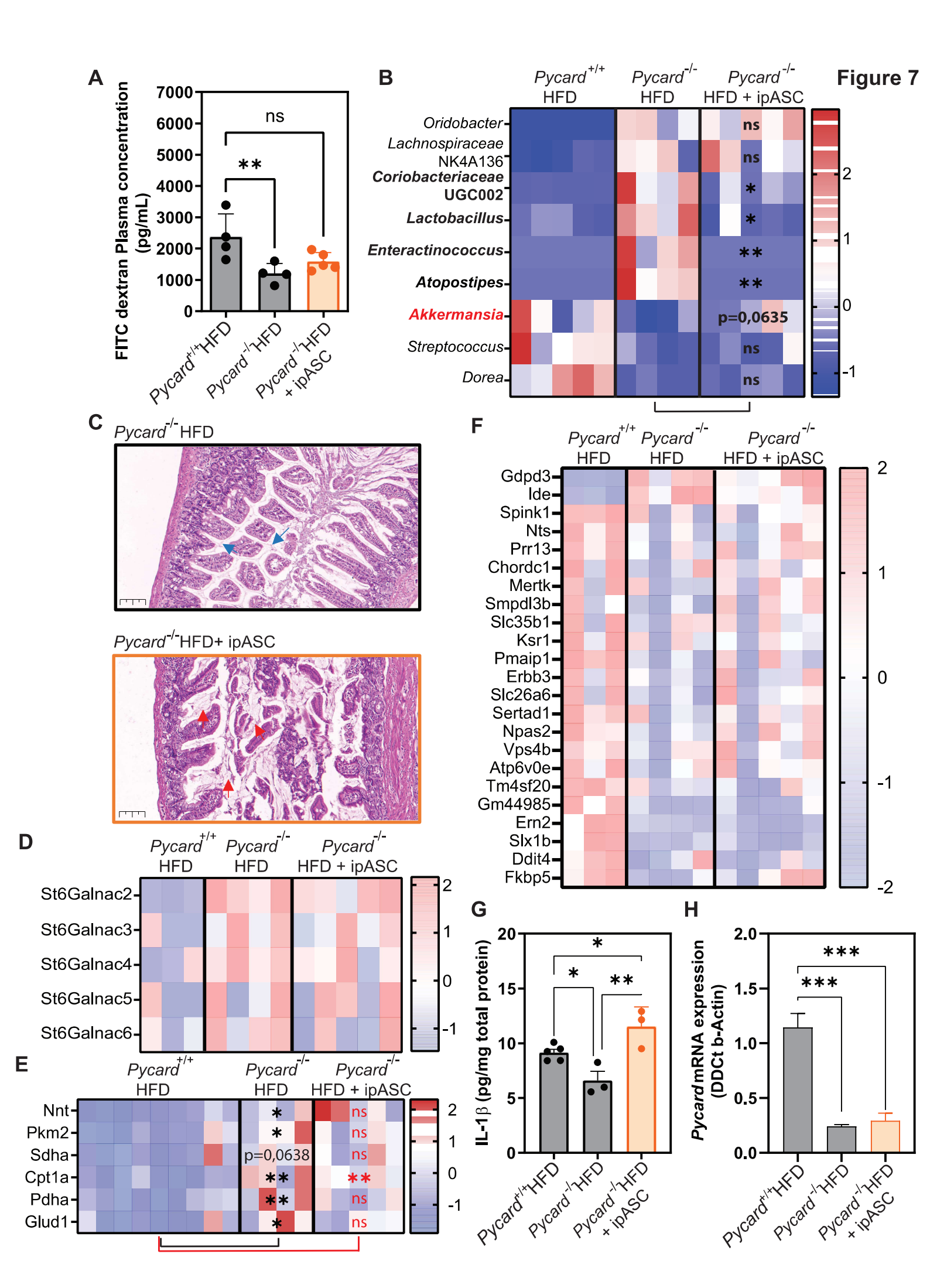
Figure 7
A
FITC dextran Plasma concentration (pg/mL)
7000
6000
5000
4000
3000
2000
1000
0
ns
**
Pycard+/+HFD
Pycard-/-HFD
Pycard-/-HFD + ipASC
B
Pycard+/+ HFD
Pycard-/- HFD
Pycard-/- HFD + ipASC
Oridobacter
Lachnospiraceae
NK4A136
Coriobacteriaceae
UGC002
Lactobacillus
Enteractinococcus
Atopostipes
Akkermansia
Streptococcus
Dorea
ns
ns
*
*
**
**
p=0,0635
ns
ns
2
1
0
-1
C
Pycard-/- HFD
Pycard-/-HFD+ ipASC
D
Pycard+/+ HFD
Pycard-/- HFD
Pycard-/- HFD + ipASC
St6Galnac2
St6Galnac3
St6Galnac4
St6Galnac5
St6Galnac6
2
1
0
-1
E
Pycard+/+ HFD
Pycard-/- HFD
Pycard-/- HFD + ipASC
Nnt
Pkm2
Sdha
Cpt1a
Pdha
Glud1
*
*
p=0,0638
**
**
*
ns
ns
ns
**
ns
ns
2
1
0
-1
F
Pycard+/+ HFD
Pycard-/- HFD
Pycard-/- HFD + ipASC
Gdpd3
Ide
Spink1
Nts
Prr13
Chordc1
Mertk
Smpdl3b
Slc35b1
Ksr1
Pmaip1
Erbb3
Slc26a6
Sertad1
Npas2
Vps4b
Atp6v0e
Tm4sf20
Gm44985
Ern2
Slx1b
Ddit4
Fkbp5
2
1
0
-1
-2
G
IL-1β (pg/mg total protein)
20
15
10
5
0
*
*
**
Pycard+/+HFD
Pycard-/-HFD
Pycard-/-HFD + ipASC
H
Pycard mRNA expression (DDCt b-Actin)
2.0
1.5
1.0
0.5
0.0
***
***
Pycard+/+HFD
Pycard-/-HFD
Pycard-/-HFD + ipASC

903 **Supplemental information**

904

905 ***Resource table.***

Reagent	Source	Identifier
Samples		
C57BL/6J (*Pycard*$^{+/+}$) mice (M. musculus)	Jackson Laboratories	RRID: IMSR_JAX:000664
ASC deficient mice in C57BL/6J background (*Pycard*$^{-/-}$)	Mariathasan et al. 2004 (71)	N/A
ASC Oligomers	Alarcón-Vila et al. 2025 (11)	N/A
Commercial		
D-Glucose	Sigma Aldrich	Cat. G7021
4Kda-FITC Dextran	Sigma Aldrich	Cat. 68059
Escherichia coli LPS 055:B5	Sigma Aldrich	Cat. L2880
Nigericin	Sigma Aldrich	Cat. N7143
MCC950	Sigma Aldrich	Cat. 5.38120
45% High-Fat-Diet	Research Diets	Cat. D12491
32% Paraformaldehyde	Sigma Aldrich	Cat. P6148
RNA later	Qiagen	Cat. 76106
Bradford Reagent	Sigma Aldrich	Cat. B6916
RTqPCR Oligomers	Sigma Aldrich	Suppl. Table 1
Mouse IL-6 ELISA Kit - Quantikine	R&D Systems	Cat. M6000B
Mouse IL-1b ELISA Kit - Quantikine	R&D Systems	Cat. MLB00C1
RNeasy mini kit	Qiagen	Cat. 74104
iScript™ cDNA Synthesis Kit	BioRad	Cat. 1708890
SYBR Premix ExTaq	Takara	Cat. RR420A
QuantSeq 3‘ mRNA-Seq V2 Library Prep Kit REV with UDI Set B	Lexogen	Cat. 225
Purelink™ Microbiome DNA Purification Kit	Thermo Fisher Scientific	Cat. A29790
Quick-16S Plus NGS Library Prep Kit	Zymo Research	Cat. D6432
E-Total	Martinez-Garcia et al. 2019 (72)	N/A

RPMI-1640 Medium liquid without L-glutamine	Sigma Aldrich	Cat. R0883
OptiMEM reduced Serum Media	Gibco	Cat. 51985-026
GlutaMAX	Thermo Fisher Scientific	Cat. 35050038
Fetal Bovine Serum (FBS)	Biowest	Cat. S181A
Penicillin-Streptomycin	Corning	Cat. 30-002-CI
Software and packages		
GraphPad Prism version 9	GraphPad Software Inc	https://www.graphpad.com/
bcl2fastq software	Illumina	https://support.illumina.com/sequencing/sequencing_software/bcl2fastq-conversion-software.html
FastQC (v0.11.9)	Brabraham Bioinformatics	https://www.bioinformatics.babraham.ac.uk/projects/fastqc/
Trimmomatic (v0.39)	Usadellab	http://www.usadellab.org/cms/?page=trimmomatic
STAR (v2.7.10a)	Dobin et al. 2012 (73)	https://code.google.com/archive/p/rna-star/
featureCounts (v2.0.3)	Subread	https://subread.sourceforge.net/featureCounts.html
R Software	R Core Team	https://www.r-project.org/
ClusterProfiler package (v4.8.1)	Bioconductor	https://bioconductor.org/packages/devel/bioc/html/clusterProfiler.html
ggplot2 (v3.4.0)	Tidyverse	https://www.tidyverse.org/blog/2022/11/ggplot2-3-4-0/
pheatmap package	Kolde el al. 2019 (67)	https://cran.r-project.org/web/packages/pheatmap/index.html
phyloseq package	McMurdie et al. 2013 (70)	https://joey711.github.io/phyloseq/install.html
Devices		
CentriVet GK Glucometer	ACON Laboratories Inc.	N/A
Synergy Mx Plate Reader	Biotek	N/A
Zeiss Axio Scope AX10	Carl Zeiss	N/A
AxioCamICC3	Carl Zeiss	N/A
NanoDrop	Thermo Fisher Scientific	N/A
iCyclerMyiQ thermocycler	BioRad	N/A

Agilent 2100 Bioanalyzer	Agilent	N/A
Qubit 4 Fluorometer	Thermo Fisher Scientific	N/A
NextSeq 2000	Illumina	N/A

906

907 **Supplemental Table 1. RT-qPCR primers sequences used in this study**

908

Name	Forward	Reverse
Actb	5' GATGTATGAAGGCTTTGGTC	5' TGTGCACTTTTATTGGTCTC
Cpt1a	5' GGGAGGAATACATCTACCTG	5' GAAGACGAATAGGTTTGAGTTC
Glud1	5' AAGACATTTGTTGTTCAGGG	5' CCAGTTCTTTTGGGTCAATC
Hmgcs2	5' AGAGCAATTTTACCACAAGG	5' TTTAAGCAGATGCTGTTTCG
Ldha	5' TGATCAAACTCAAAGGCTACACA	5' TTCCTCAGAAGTCAGAGTCACCT
Nnt	5' TTCTGGTGACTCAGAGAATG	5' CCAGGTACATGATTTCTTCG
Pdha	5' GGTAGATGGAATGGATATCTTG	5' TACTTCCTGGATTTCTTCTCG
Pgc1a	5' TCCTCTTCAAGATCCTGTTAC	5' CACATACAAGGGAGAATTGC
Pkm	5' CAGGTTTGATGAGATCTTGG	5' CTTCTTGATCATGCTCTCC
Pycard	5' AATTTAACATGGGTTTCCCC	5' AGTTTGTCTTCAAGCTTCTG
Sdha	5' GAATTTGTTCAGTTCCACCC	5' ATCTCAAGAGTCATGGATCG

909
910
911
912
913
914
915
916
917

918 **Supplemental Figure Legends**

919

920 **Supplemental Figure 1. High fat diet increases glucose tolerance and body weight.**

921 **A.** Body weight on wild type (*Pycard*$^{+/+}$) mice fed for 5 months under normal chow diet (NCD,
922 grey, n=4) or high fat diet (HFD, blue, n=5).

923 **B.** Glucose tolerance (left) and area under the curve (AUC, right) in wild type mice treated as in
924 A.

925 **C, D.** Interleukin (IL)-1β (C), and IL-6 (D) release from peritoneal cells collected from wild type
926 (*Pycard*$^{+/+}$, n=4, grey) or *Pycard*$^{-/-}$ (n=4, white) mice fed for 5 months with a NCD and in vitro
927 stimulation as indicated in the figure (LPS: lipopolysaccharide; NIG: nigericin, MCC: MCC950).
928 Columns represent the mean of each condition and error bars represent SEM. Two-way ANOVA
929 with multivariant Sidak's test was used for A, B (left panel) and C. Mann-Whitney test was used
930 for B right panel (ns, $p>0.05$; *$p\leq0.05$; **$p\leq0.01$; *** $p\leq0.001$).

931

932 **Supplemental Figure 2. HFD induces dysbiosis and compromises gut epithelial protection.**

933 **A-C.** Relative abundance of the total faecal microbiota at class level (A, B), and of *Akkermansia*
934 (C) on wild type (*Pycard*$^{+/+}$) mice fed with a normal chow diet (NCD, n=4) in comparison with
935 high fat diet (HFD, n= 5).

936 **D.** Intestinal permeability measured by 4 kDa FITC-dextran in *Pycard*$^{+/+}$mice treated as in A-C.

937 **E,F.** Haematoxylin and eosin histology of the small intestine of *Pycard*$^{+/+}$ mice fed for 5 months
938 with a NCD representative of n=4 (E) or HFD representative of n= 5 (F). Scale bar: 200 μm.
939 Each dot represents a distinct animal, bars represent the mean, error bars represent SEM. Unpaired
940 *t*-test was used for C, D (*$p\leq0.05$; **$p\leq0.01$).

941

942 **Supplemental Figure 3. Cohousing partially restored wild type-dependent microbiota profile**
943 **after HFD in *Pycard*$^{-/-}$ mice.**

944 **A-C.** Relative microbiota abundance at family's level of class on wild type (*Pycard*$^{+/+}$, n=4) or
945 *Pycard*$^{-/-}$ mice (n=4) in normal chow diet (NCD) and genotype single housed (A) or cohoused (B)
946 mice, and on cohoused mice after 3 months of high fat diet (HFD) (C).

947

948 **Supplemental Figure 4. ASC deficiency increases regulation of inflammatory pathways in**
949 **the small intestine during high fat diet.**
950 Extended vision of the Gene Ontology differential expressed pathways in the small intestine of
951 wild type (*Pycard*$^{+/+}$, right column) and *Pycard*$^{-/-}$ (left column) mice fed for 5 months with a high
952 fat diet (HFD). Color represents adjusted p value, and size the number of genes (count).
953
954 **Supplemental Figure 5. High fat diet induces liver steatosis and inflammation.**
955 **A, B.** Haematoxylin and eosin histology of the liver of wild type (*Pycard*$^{+/+}$) mice fed for 5 months
956 with a normal chow diet (NCD) (A) or a high fat diet (HFD) (B). Scale bar: 200 μm.
957 **C, D.** Interleukin (IL)-1β (C) and IL-6 (D) in the liver of wild type (*Pycard*$^{+/+}$, grey, n=7) or
958 *Pycard*$^{-/-}$ (white, n=2) mice fed for 5 months with an NCD.
959 Each dot represents a distinct animal, bars represent the mean, error bars represent SEM. Mann-
960 Whitney's test (ns, p>0.05).
961
962 **Supplemental Figure 6. Intestinal microbiota after intraperitoneal administration of**
963 **recombinant ASC oligomers during high fat diet.**
964 **A-C.** Relative microbiota abundance at class level (A), Akkermansiaceae (B) and Lachnospiraceae
965 (C) families on feces of wild type (*Pycard*$^{+/+}$, n=5), *Pycard*$^{-/-}$ (n=4) or *Pycard*$^{-/-}$ mice treated with
966 intraperitoneal injection of recombinant ASC oligomers (ipASC, orange, n=4) fed for 5 months
967 with high fat diet (HFD).
968 Each dot represents a distinct animal, bars represent the mean, error bars represent SEM. One-way
969 ANOVA with multivariant Holm-Sidak's test, all comparison presented a p>0.05 (ns).
970
971 **Supplemental Figure 7. Intraperitoneal administration of recombinant ASC oligomers did**
972 **not affect glucose tolerance, peritoneal inflammation or hepatic damage.**
973 **A.** Body weight from wild type (*Pycard*$^{+/+}$, grey, n=5), *Pycard*$^{-/-}$ (black, n=4), and *Pycard*$^{-/-}$ with
974 intraperitoneal injection of recombinant ASC oligomers (+ipASC, orange, n=5) mice fed for 5
975 months with a high fat diet (HFD).
976 **B.** Glucose tolerance in mice treated as in A.
977 **C, D.** Haematoxylin and eosin histology of the liver of mice treated as in A. Scale bar: 200 μm.
978 **E.** IL-1β in the liver from mice treated as in A.

979 **F.** Relative hepatic gene expression in mice treated as in A.

980 Each dot represents a distinct animal, bars represent the mean, error bars represent SEM. Two-
981 way ANOVA and multivariant Sidak's test was used for A-B. One-way ANOVA and multivariant
982 Holm-Sidak's test was done for G, H (ns, $p>0,05$; *$p\leq0.05$; **$p\leq0.01$; *** $p\leq0.001$).

Supplemental Figure 1

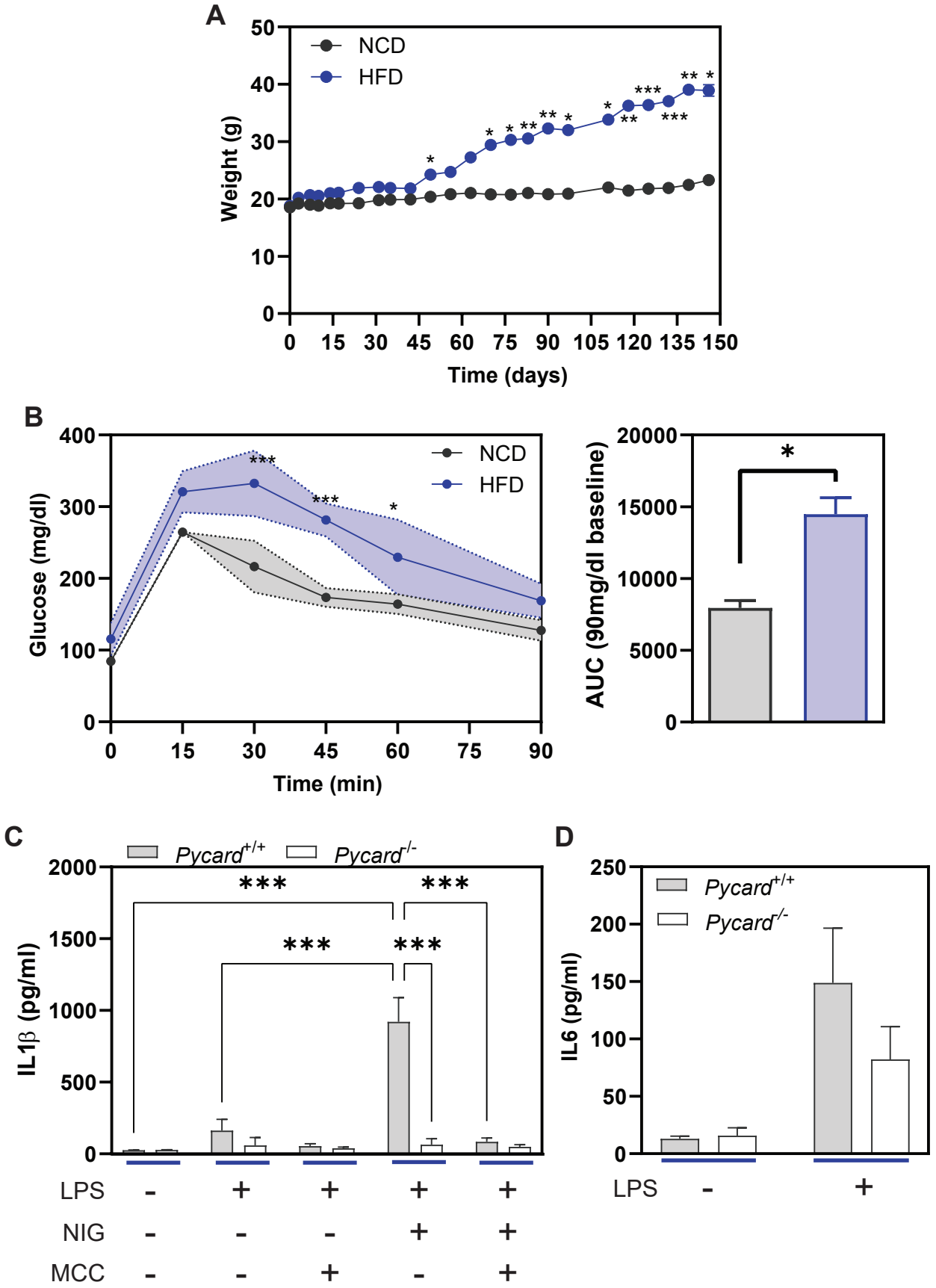

Supplemental Figure 2

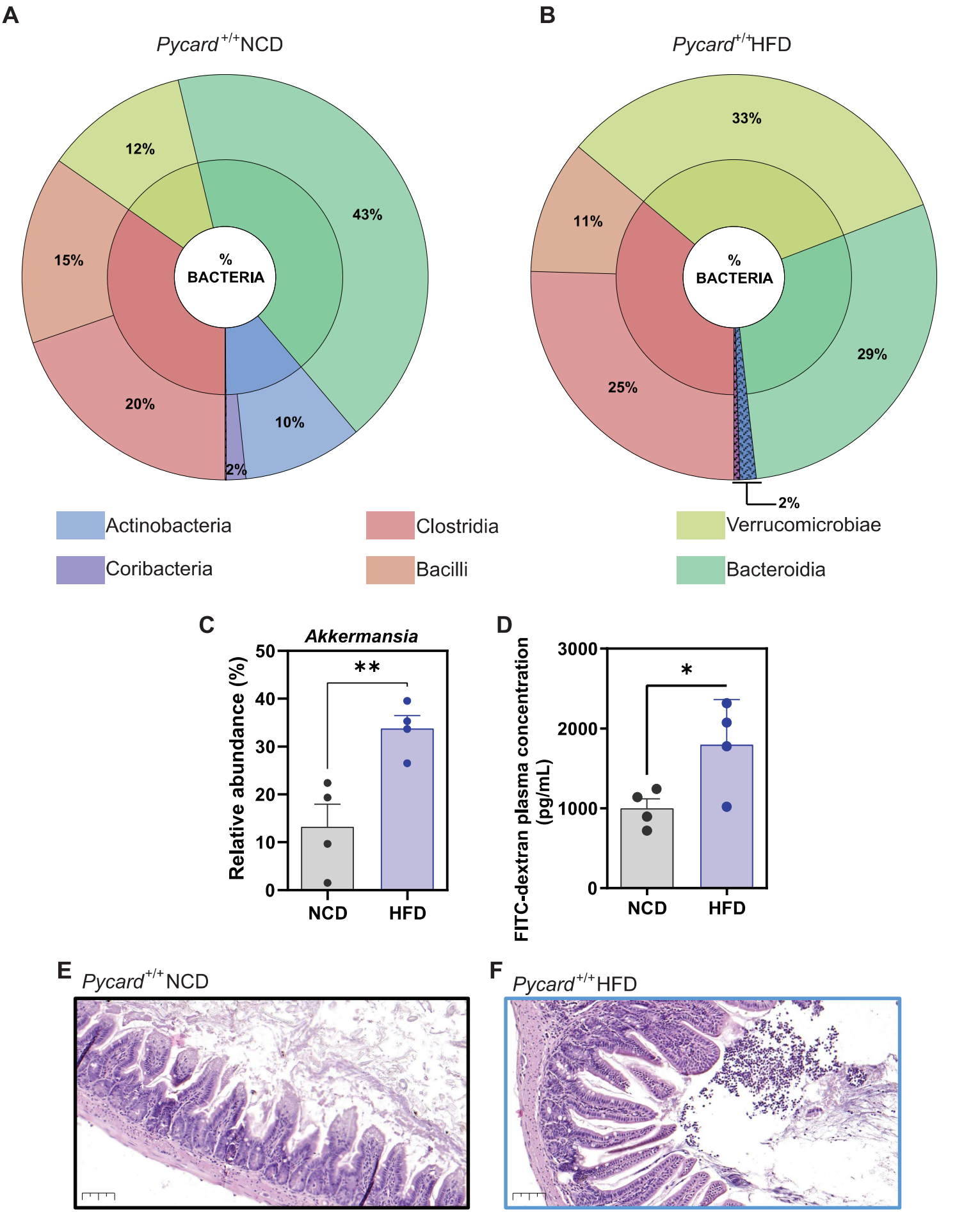

Supplemental Figure 3

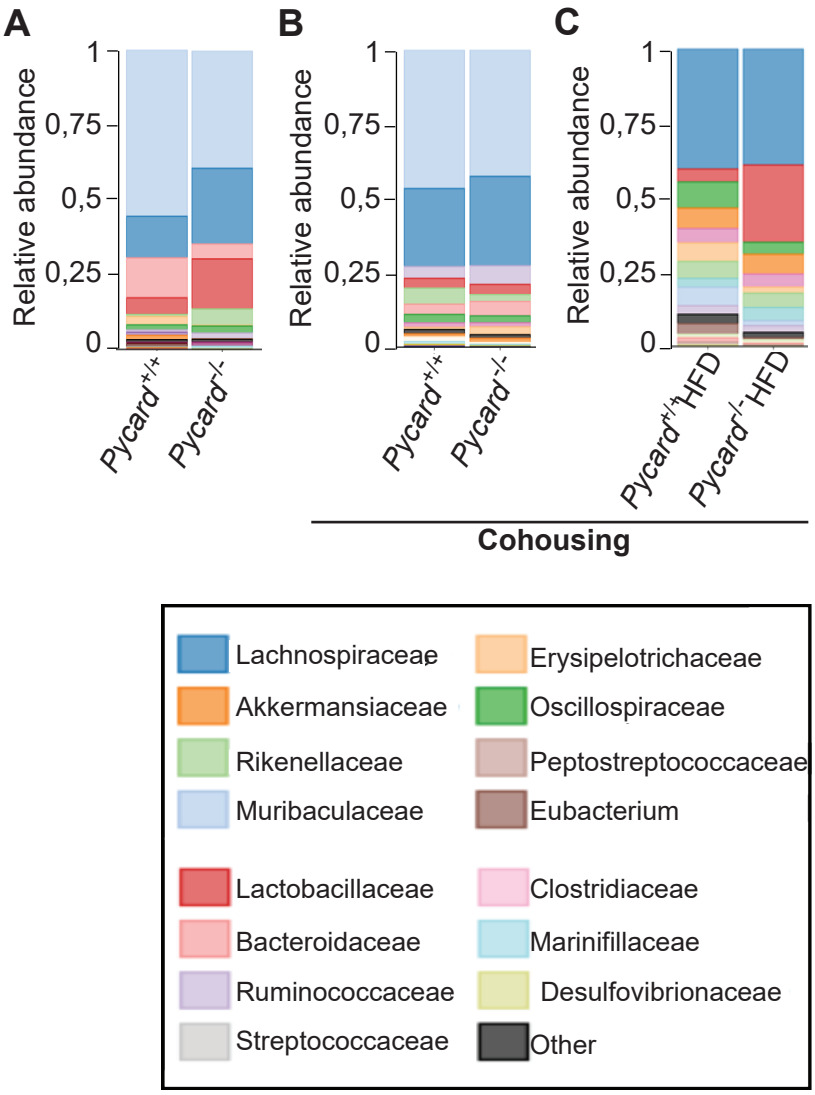

Supplemental Figure 4

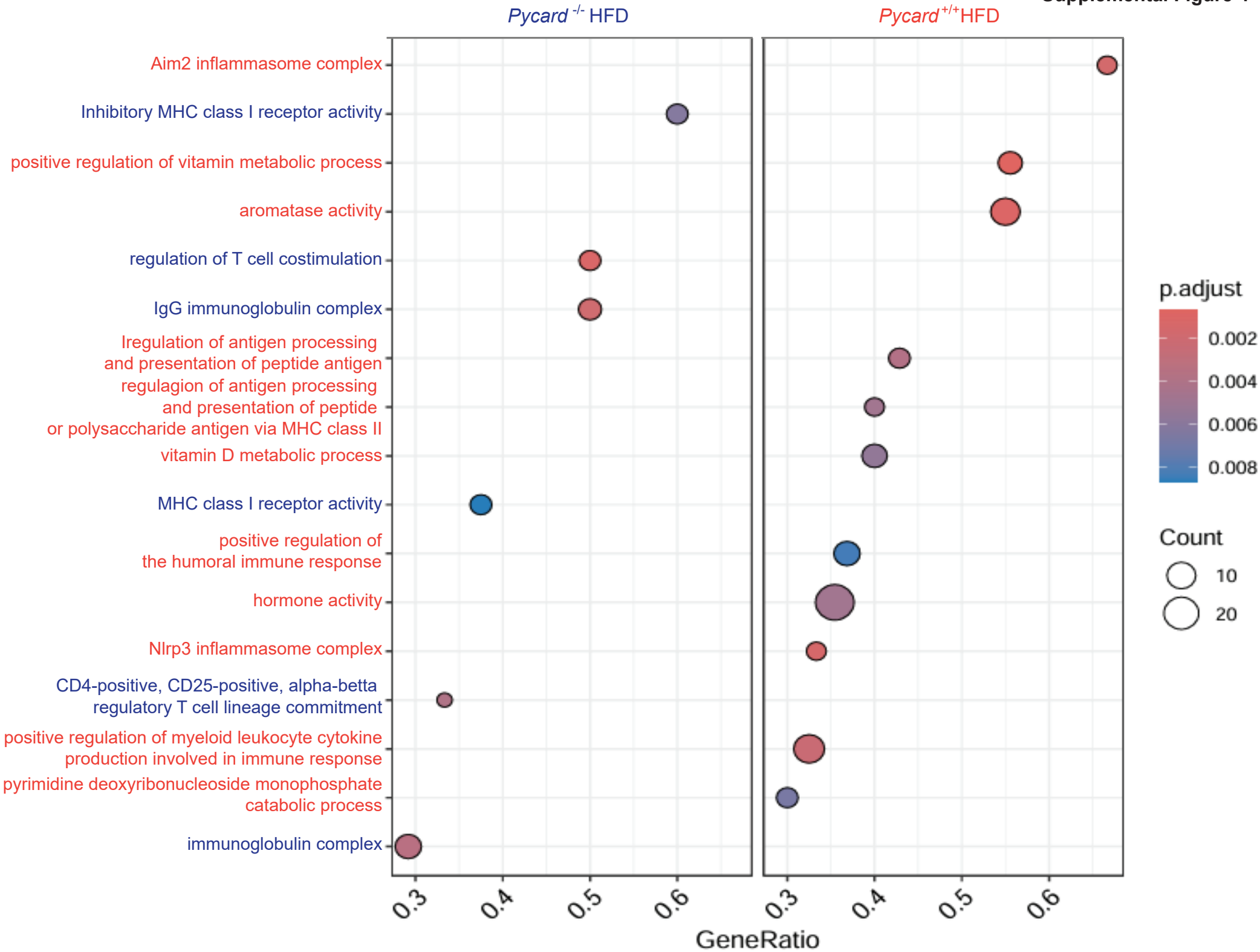

Supplemental Figure 5

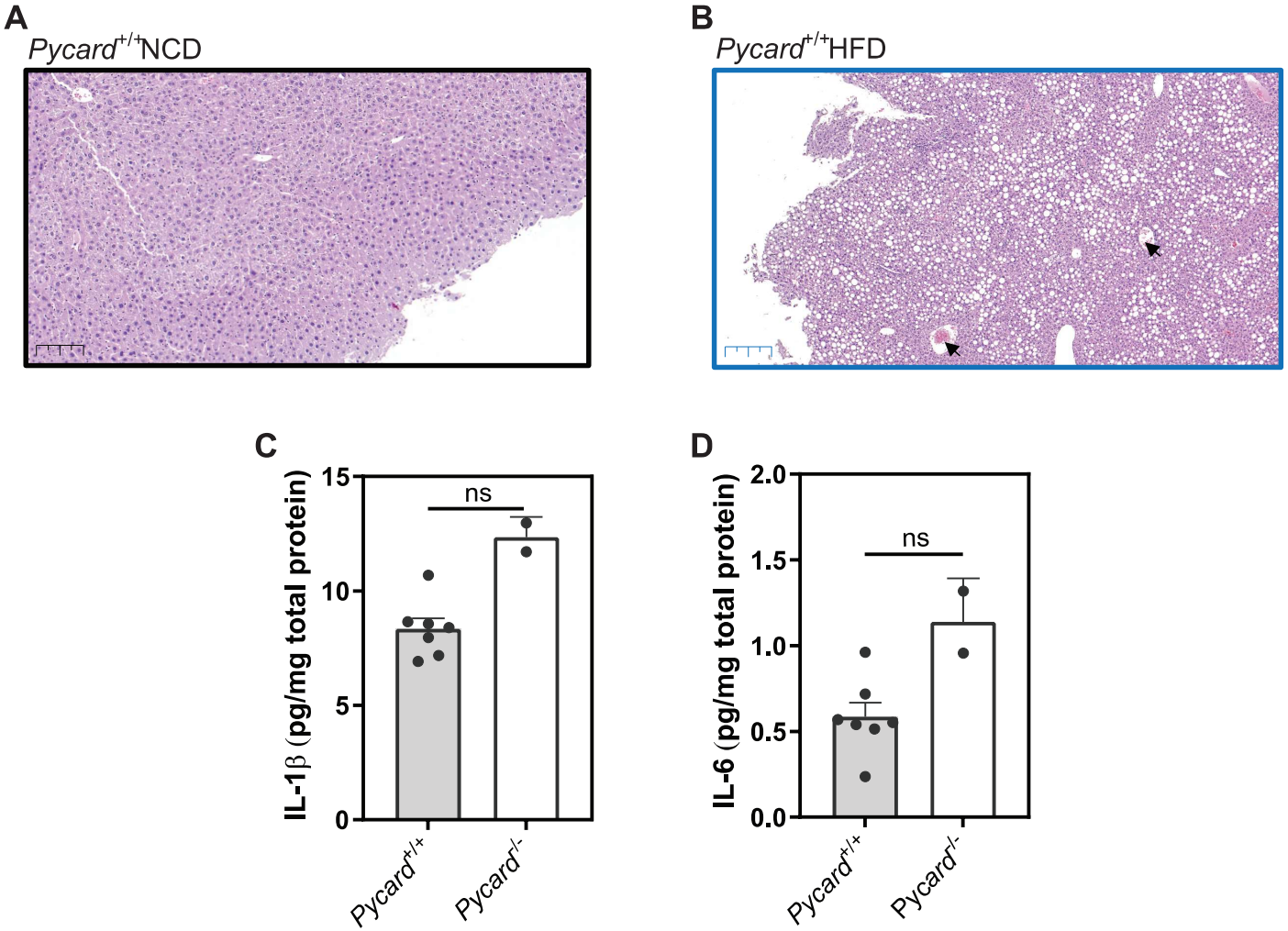

Supplemental Figure 6

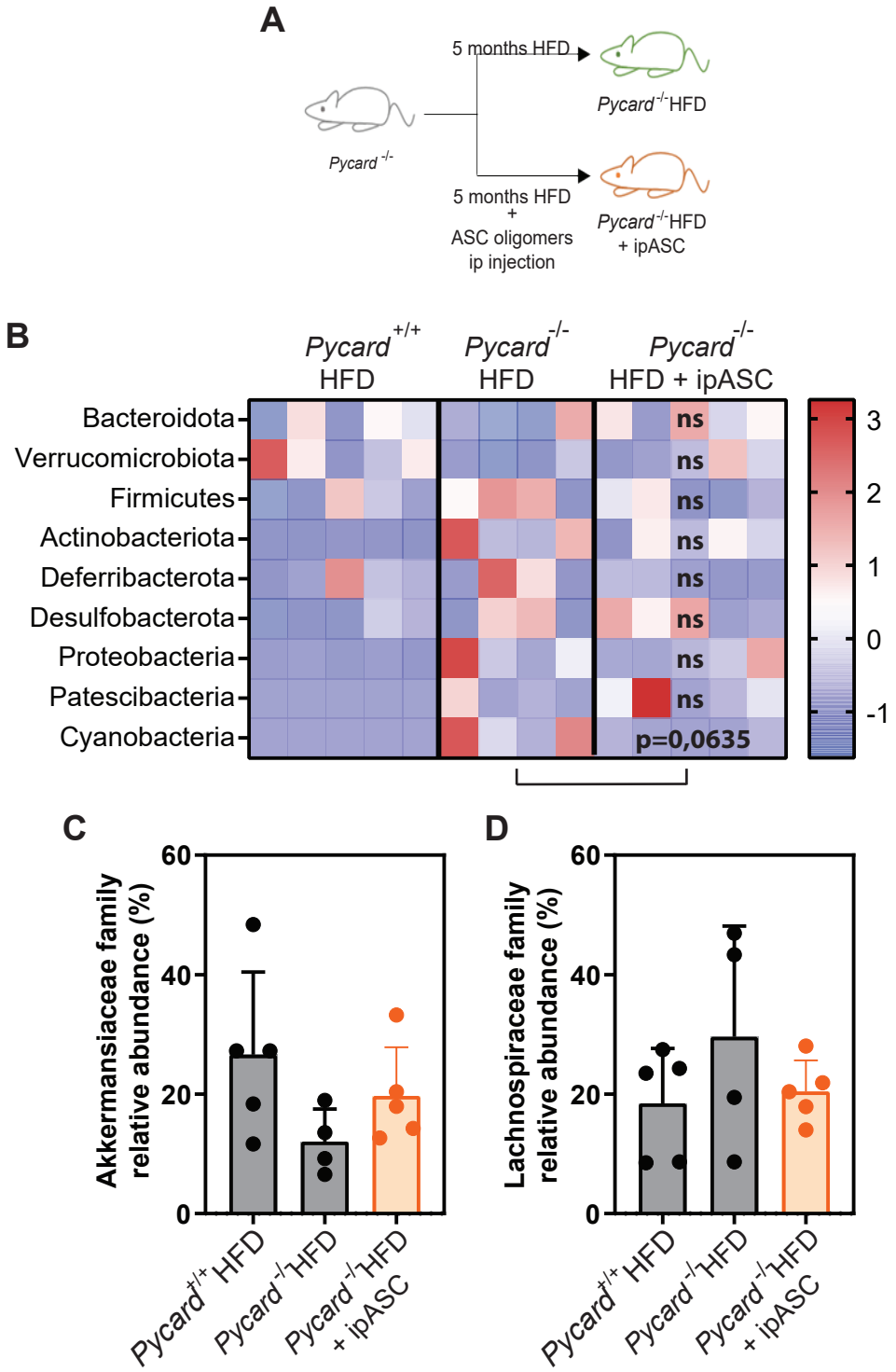
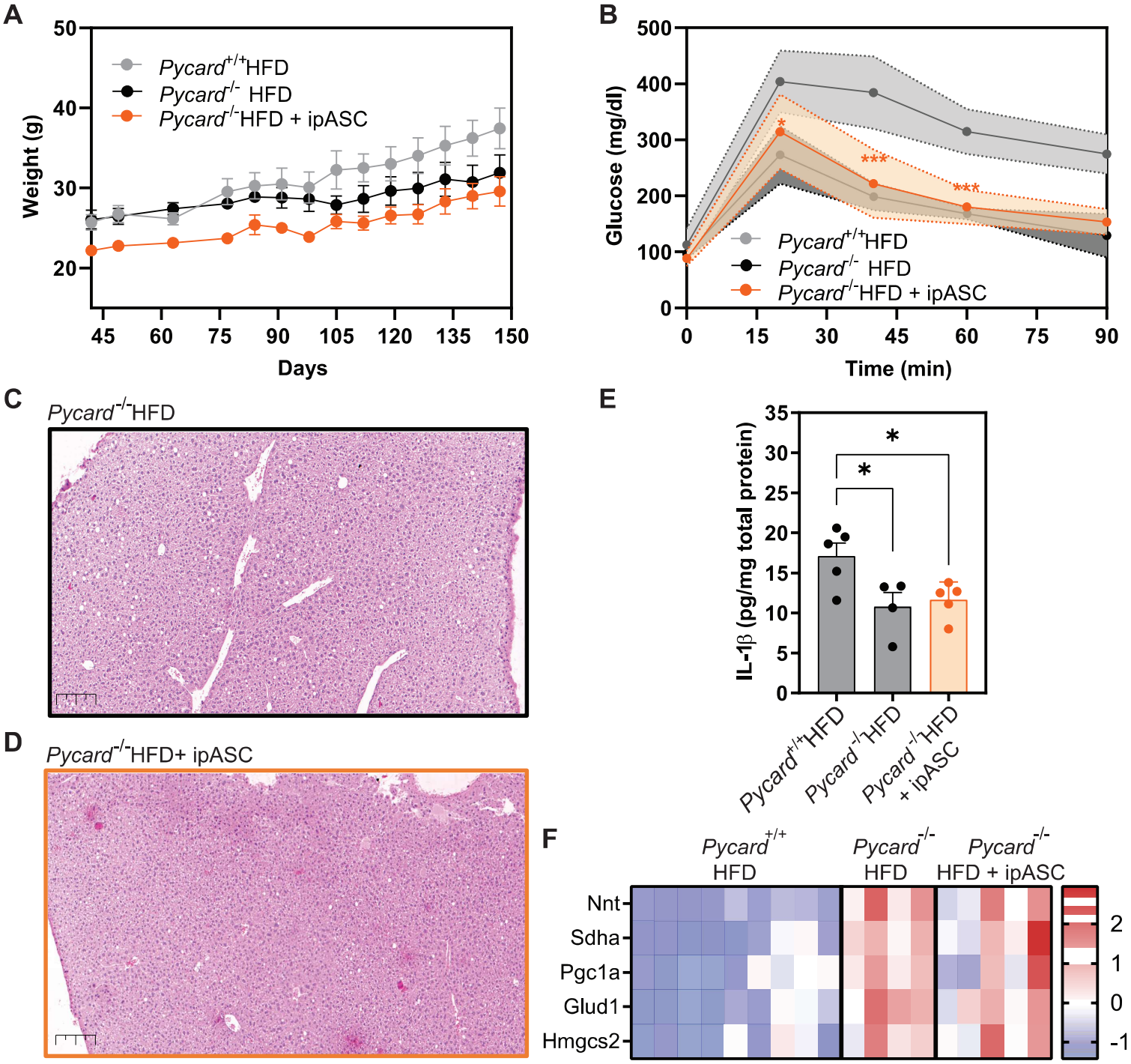
Supplemental Figure 7